

POLITECNICO DI TORINO

**Corso di Laurea Magistrale
Mechatronic engineering**

Tesi di Laurea Magistrale

**Optimization-based reconstruction of
electromagnetic fields from UAV
measurements**



Relatore

Prof. Giuseppe Vecchi

Correlatori

Prof. Fabrizio Dabbene

Dott. Righero Marco

Candidato

Emanuele Raffaele Riccardi

246382

ANNO ACCADEMICO 2018-2019

ACKNOWLEDGEMENT

Vorrei iniziare col ringraziare coloro che mi hanno dato l'opportunità di poter lavorare a questo progetto di tesi. Grazie al professor Vecchi ed al professor Dabbene a loro va la mia gratitudine.

Ringrazio coloro che mi hanno seguito e consigliato in questa attività. Grazie a Marco Righero, Chiara Ravazzi e Lorenzo Ciorba.

Grazie di nuovo a Marco Righero che ha avuto la pazienza di seguirmi quotidianamente, spiegandomi con calma gli errori fatti durante il lavoro ed aiutandomi fino alla fine. Grazie.

Ringrazio la mia famiglia, che con molti sforzi e sacrifici mi ha permesso di poter studiare a Torino, supportandomi sempre in qualsiasi situazione.

Ringrazio Giuliana, colei che ormai da 5 anni mi è sempre vicino. Sei sempre stata il mio supporto in ogni occasione, non lasciandomi mai da solo. Grazie.

Ringrazio Lazzaro, sempre un Amico a cui affidarsi in caso di bisogno.

Ringrazio i miei amici del Politecnico, Benedetta, Marco, Stefano e Francesco; grazie a voi è stato più piacevole studiare.

Ringrazio i miei amici napoletani a Torino. Grazie ad Alessandra, Vincenzo e Raffaele, insieme a Lazzaro mi avete spesso aiutato a superare la nostalgia di casa.

Ringrazio i miei amici di Napoli. Grazie a Marco ed Antonio che seppur lontani mi sono sempre stati vicini.

Infine, ringrazio tutti coloro che mi hanno regalato un sorriso e mi son stati vicini, permettendomi di raggiungere questo traguardo che fine a qualche anno fa sembrava impossibile.

Contents

1	INTRODUCTION	11
2	REVIEW	13
2.1	WHAT IS AN ANTENNA	13
2.2	ELECTROMAGNETIC FIELD RADIATED BY AN ANTENNA	16
2.3	ANTENNA UNDER TEST	23
3	CVX SOFTWARE	29
3.1	THIN PLATE SPLINE	30
3.2	NUCLEAR NORM MINIMIZATION	32
3.3	ALGORITHM	34
3.4	PATH OF THE DRONE	35
3.5	SIMULATION AND ANALYSIS	38
3.5.1	RESULTS RADIAL PATH CVX	40
3.5.2	RESULT SPIRAL PATH CVX	43
3.5.3	RESULT RECTANGULAR PULSE FLIGHT CVX	45
4	SINGULAR VALUE THRESHOLDING	47

4.1	THE ALGORITHM	48
4.2	RADIAL PATH SVT	51
4.3	SPIRAL PATH SVT	55
4.4	COMPARISON BETWEEN SVT AND CVX	57
5	REDUCED ORDER MODEL	65
5.1	LOVE'S THEOREM	66
5.2	REDUCED ORDER MODEL METHOD	68
5.3	DISCRETE EMPIRICAL INTERPOLATION	70
5.3.1	CUBIC SPLINE AND B-SPLINE TRAJECTORY	73
5.4	RECONSTRUCTED NEAR FIELD	75
5.4.1	REGULAR SURFACE	76
5.4.2	IRREGULAR SURFACE	82
5.5	RECONSTRUCTED FAR FIELD	93
6	CONCLUSION	109
	Bibliography	111

List of Figures

2.1	Spherical reference frame	14
2.2	Example of an array of antennas used for tv receiving signal	17
2.3	How the waves propagates in the 3 different regions. Credits to physics.stackexchange.com	23
2.4	Picture of a helix antenna	23
2.5	Single antenna layout and simulated field	25
2.6	Array 2x2 layout and simulated field	26
2.7	Array 3x3 layout and simulated field	26
2.8	Array 4x4 layout and simulated field	27
3.1	Example of an uniforme lattice Ω , 80x80, where 1600 samples are randomly selected.	31
3.2	Example of how the linear map and its complementary work	35
3.3	Example of radial pattern where $\theta_0=15^\circ$	36
3.4	Example of spiral pattern, where $A=0.1$ and $\omega=1.3$	37
3.5	Example of a rectangular pulse flight	38

3.6	Difference between the simulated and the interpolated field. $\theta_0 = 15^\circ$, radial path	42
3.7	Difference between the simulated and the interpolated field. $\alpha = 0.1$, radial path	42
3.8	Difference between the simulated and the interpolated field. $\omega = 1.1$, spiral path	44
3.9	Difference between the simulated and reconstructed field. $\omega = 1.1$ $\alpha = 1$, spiral path	44
4.1	Measured points setting $\theta_0=15^\circ$	52
4.2	Layout of the array 4x4 of helix antennae	52
4.3	Reconstructed field with the SVT, 4x4 array, $\lambda/5$ sampling	54
4.4	Original and reconstructed field, svt, radial path, 20% of points, $\lambda/10$ sampling	60
4.5	Measured points setting $A=0.15$ and $\omega=1.3$	61
4.6	Reconstructed field with the spiral path, $\lambda/5$	62
4.7	Reconstructed field with the spiral path, $\lambda/10$, 20% of points	63
4.8	Graphics that shows the behaviour of the results obtained using the CVX software	64
4.9	Graphics that shows the behaviour of the results obtained using the SVT algorithm	64
5.1	Starting condition of the Love's theorem	66
5.2	Final condition of the Love's theorem	67
5.3	Scheme of input-output for the ROM	69
5.4	Example of the points selected by the DEIM	72

5.5	Difference between cubic spline and B-spline	76
5.6	Behaviour of the error computed as (5.1) for different cases	78
5.7	Example of uniform $\lambda/2$ sampling	79
5.8	Original field, array 4x4, ROM	80
5.9	Reconstructed NF, spiral path 15% of points, 4x4, ROM	80
5.10	Reconstructed NF, radial path 15% of points, 4x4, ROM	81
5.11	Reconstructed NF, all points of the DEIM, 4x4, ROM	81
5.12	Reconstructed NF, joining all points of the DEIM, 4x4, ROM	82
5.13	Reconstructed NF, uniform sampling $\lambda/2$, 4x4 ROM	82
5.14	Difference between a regular and irregular surface	83
5.15	Irregular surface in the case of a uniform $\lambda/2$ sampling	85
5.16	Spiral trajectory of 140m regular surface	86
5.17	Error for irregular and regular surface, spiral trajectory	86
5.18	Original NF and reconstructed NF for cubic spline	87
5.19	Original NF and reconstructed NF for B-spline	88
5.20	Original NF and reconstructed NF for radial trajectory 140m	89
5.21	Original NF and reconstructed NF for radial trajectory 173m	90
5.22	Original NF and reconstructed NF for spiral trajectory 140m	91
5.23	Original NF and reconstructed NF for spiral trajectory 173m	92
5.24	Circular Polarization	94
5.25	Original FF and reconstructed FF for a uniform $\lambda/2$ sampling	95
5.26	Original FF and reconstructed FF for B-spline trajectory	96
5.27	Original FF and reconstructed FF for spiral trajectory, 140m	97
5.28	Original FF and reconstructed FF for radial trajectory, 140m	98
5.29	Original FF and reconstructed FF for cubic trajectory	99

5.30	Original FF and reconstructed FF for spiral trajectory, 173m . . .	100
5.31	Original FF and reconstructed FF for radial trajectory, 173m . . .	101
5.32	Original FF and reconstructed FF for B-spline trajectory, single antenna	102
5.33	Original FF and reconstructed FF for B-spline trajectory, array 2x2	103
5.34	Original FF and reconstructed FF for B-spline trajectory, array 3x3	104
5.35	Original FF and reconstructed FF for cubic spline, single antenna .	105
5.36	Original FF and reconstructed FF for cubic spline, array 2x2 . . .	106
5.37	Original FF and reconstructed FF for cubic spline, array 3x3 . . .	107

List of Tables

2.1	Error computed as (5.4) for different cases, lenght trajectory 140m	24
3.1	Variation of the error with respect to θ_0 , radial trajectory, CVX . .	41
3.2	Variation of the error with respect to α , when $\theta_0 = 15^\circ$	41
3.3	Variation of the error with respect to ω , spiral trajectory CVX . .	43
3.4	Variation of the error with respect to α , spiral trajectory, $\omega = 1.1$.	43
3.5	Variation of the error with respect to the amplute, rectangular pulses flight	45
3.6	Variation of the error with respect to α , amplitude =3, rectangular pulses flight	45
4.1	Variation of (4.8), [%], wrt τ and δ	53
4.2	Variation of (4.7), [%], wrt τ and δ	53
4.3	Variation of the error considering an error, SVT, radial	53
4.4	Variation of the error wrt percentage of measured points, svt, radial path	55
4.5	Variation of (4.8), [%], wrt τ and δ , spiral path	56
4.6	Variation of (4.7), [%], wrt τ and δ , spiral path	56

4.7	Variation of the error considering an error, SVT, spiral	56
4.8	Variation of the error wrt percentage of measured points, svt, spiral path	57
4.9	CVX and SVT error, spiral path	58
4.10	CVX and SVT error, radial path	58
4.11	CVX and SVT error, random selection	59
5.1	Error computed as (5.4) for different cases	78
5.2	Error computed as (5.4) for different cases, lenght trajectory 140m	84
5.3	Error computed as (5.4) for different cases, lenght trajectory 173m	84
5.4	Error computed as (5.4) in the case of a uniform $\lambda/2$ sampling . .	85
5.5	Error computed as (5.4) spiral trajectory on regular surface	85
5.6	Error computed as (5.4) for cubic and B-spline considering all the points of the DEIM	93

Chapter 1

INTRODUCTION

This thesis talks about the reconstruction of the near and far field radiated by different configurations of arrays of antennae starting from the measurement of a few samples in the near field region of the scattering object. The samples are supposed to be measured in external environment by means of UAV drone. The works has been structured in this way:

- The second chapter contains a brief introduction to the world of the electromagnetism, introducing the Maxwell's equations since to arrive to the difference of the near and far field radiated by an antenna; moreover, there is a short introduction to the parameters that are able to describe an antenna. It concludes by introducing what is the antenna under test taken into account in this thesis, its parameters and the simulated radiated near field on a measurement surface that can be represented by a matrix;
- The third chapter talks about the first method studied here in order to reconstructed the near field scattered by the an antenna, on a regular constant

surface measurement. The method relies on a first interpolation through splines for the points of the matrix that are not measured by the drone, and a successive use of the CVX software for minimizing the nuclear norm of the unknown matrix;

- The fourth chapter talks about the second method studied in order to improve the drawbacks of the previous one. It relies on the use of Singular Value Threshold algorithm to minimize the nuclear norm of the unknown matrix. The chapter ends with a comparison between the two methods;
- The methods seen in the previous chapters are both based on matrix completion algorithms. Instead, the new method introduced in the chapter five relies on the computation of the equivalent currents, that belongs to a generic surface S that encloses the antenna under test. By the knowledge of the equivalent currents it is possible to compute both the near and the far field radiated by the antenna. Moreover, here will be considered even an irregular surface measurement, coincident with the trajectory of the drone;
- The last chapter is a conclusion of all the work carried out with an analysis of the results.

Chapter 2

REVIEW

The main purpose of the thesis is the interpolation of the electromagnetic field without prior information on the radiating source, using measurements acquired by UAV (drones). Before to start to discuss about the main work, a brief introduction about the theory and the notations used in the following chapter is necessary.

2.1 WHAT IS AN ANTENNA

In the thesis, the analyzed antenna under test is an array of antennae of different sizes. An antenna is a device that can work both as a transmitter and as a receiver. In the former case, the purpose is to radiate the electromagnetic power coming from a generator into the space; in the latter case, the aim is to receive the electromagnetic power coming from the space and to transfer it to a load .In theory, both cases must be analysed to study the complete behaviour of an antenna but,

as a consequence of the Maxwell's equations, a relation exists between the antenna working as transmitter and the same antenna working as receiver [1]. So, once the behaviour in one case is known, it is easy to obtain the behaviour in the other way. Depending on the working frequency, or more in general, on the asked requirements, there are various types of antenna. A detailed description is out of the scope of this thesis, but more information can be found in the book in literature [2].

The description of antenna, that is the way it works as a receiver and the way it works as a transmitter, is completely fulfilled by two parameters: the gain and the directivity.

The directivity describes how the intensity of the radiating field changes in each direction. They are introduced for a spherical reference frame, as in Figure 2.1; r is the radius of the sphere, θ the longitudinal angle and ϕ the latitudinal angle. The directivity depends only on the two angular coordinates θ and ϕ .

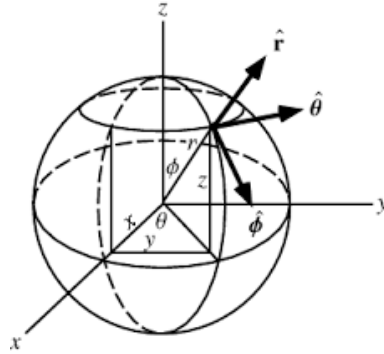


Figure 2.1. Spherical reference frame

The directivity is defined as the limit of the radius r tending to infinity of the ratio between the power density radiated in a considered direction and the average

power density radiated into the space:

$$D(\boldsymbol{\theta}, \phi) = \lim_{r \rightarrow \infty} \frac{|\mathbf{E}(\mathbf{r}, \boldsymbol{\theta}, \phi)|^2 \backslash 2\zeta}{Pow_{rad} \backslash A} \quad (2.1)$$

In the equation (2.1) $D(\boldsymbol{\theta}, \phi)$ is the directivity function, $|\mathbf{E}(\mathbf{r}, \boldsymbol{\theta}, \phi)|^2$ represents the square of the absolute value of electric field radiates into the considered direction, ζ is the impedance of the medium, Pow_{rad} is the value of the power radiated into all the space, A is the surface of the sphere that the power goes through.

From a physics point of view, the directivity tells about how strong is the intensity of the radiated field in a certain direction with respect to the average value. In most cases designers are interested in the direction where the directivity assumes its maximum value, so refereeing to directivity only is always intended the direction of the maximum value. Much an antenna radiates more power only in one direction much this value is bigger [3].

The gain is a parameter that relates the power that an antenna radiates in a certain direction with respect of the power radiated by an ideal isotropic radiator, i.e. a radiator with no internal losses, in the same direction. The mathematical formula of the gain function, $G(\boldsymbol{\theta}, \phi)$, is basically similar to (2.1). The difference is at the denominator, where instead of the value of Pow_{rad} , in this case there is the value of Pow_{in} , that is the power received by the antenna.

$$G(\boldsymbol{\theta}, \phi) = \frac{|\mathbf{E}(\mathbf{r}, \boldsymbol{\theta}, \phi)|^2 \backslash 2\zeta}{Pow_{in} \backslash A} \quad (2.2)$$

These two a-dimensional parameters are strictly related to the size of the antenna, for exception of superdirectivity antennas [4].

The directivity of the antenna is something related to the ratio between the size of the antenna and its wavelength λ , $\lambda = \frac{c_0}{f}$, where c_0 is the speed of the light while f is the angular frequency.

It is worth noticing that if the requirement of a project is to have a high directivity antenna, the solutions are or the increasing of the working frequency or the increasing of the size of the antenna itself [5].

In several applications, the range of the frequency can't overcome a certain value, so in order to obtain a high directivity antenna it is necessary to increase the size. Another solution is given by considering a group of antennas, called array. In general, all the elements of an array of antennas are of a common type, aligned on a line or in a plane [6]. By positioning all the antennas composing the array in a proper way, high value of directivity can be reached with the advantage to keep the size of each antenna reasonable small. An array of antennas, for example, it is used for the reception of TV signal.

2.2 ELECTROMAGNETIC FIELD RADIATED BY AN ANTENNA

In this section there is a brief introduction regarding the Maxwell's equations and how antenna propagates into the free space.

The starting point in order to compute the equation of the electric and of the magnetic field radiated by an antenna are the Maxwell's equations, that represent a set of four partial differential equations. They link the electromagnetic fields to the magnetic and electric sources [7].

There are two different formulations: the microscopic Maxwell's equations that



Figure 2.2. Example of an array of antennas used for tv receiving signal

describe what happens at atomic scale; the macroscopic Maxwell's equations that describe what happens a large scale, neglecting what happens at atomic scale, for example the quantum phenomena.

Since there are differential equations, to find a unique solution boundary and initial conditions must be known. A detailed method about how imposing correctly boundary conditions is described by P. Monk in his book [8].

In this thesis, a particular solution of the Maxwell's equations in the frequency domain has been used, known as spherical waves function [9].

$$\left\{ \begin{array}{l} \nabla \times \mathbf{H} = -i\omega\epsilon\mathbf{E} + \mathbf{J} \\ \nabla \times \mathbf{E} = -i\omega\mu\mathbf{H} - \mathbf{M} \\ \nabla \cdot \epsilon\mathbf{E} = \rho \\ \nabla \cdot \mu\mathbf{H} = 0 \end{array} \right. \quad (2.3)$$

In the equation (2.3), the vectors \mathbf{E} and \mathbf{H} are respectively the electric and the magnetic field, \mathbf{J} and \mathbf{M} are the vectors of the electric and magnetic current density, ω is the angular frequency, ϵ and μ are the permittivity and the permeability of the medium, ρ the volume charge density.

The aim is to derive the expression of the electric and magnetic field. For hypothesis, the sources propagate toward a medium that has this characteristic:

- If there are many sources applied to the system, the overall effect is the sum of each effect produced by one single cause, i.e. the medium is linear;
- The permittivity (ϵ) and the permeability (μ) of the material are constant in all the volume of the material and constant in time, i.e. the medium is homogenous;
- The vectorial properties of the permittivity and of the permeability are not described by tensors but they are the same in each point, i.e. the medium is isotropic.

Furthermore, since we are dealing with the Maxwell's equations in the frequency domain, it is possible to work even with dispersive media.

Instead of solving directly the equation, an alternative and easy manner is to describe the electric and magnetic field in terms of two auxiliary quantities, a

vector potential and a scalar potential [10].

From the last equation of the set (2.3) comes out that exists at least one vector potential (\mathbf{f}) that allows to write the magnetic field as the rotor of the vector potential itself; this is possible since the divergence of the magnetic field is null. So:

$$\exists | \mathbf{f} : \quad \mu \mathbf{H} = \nabla \times \mathbf{f} \quad (2.4)$$

By substituting the equation (2.4) in the second equation of the set (2.3), since for hypothesis the medium is considered linear and the curl operator is linear, neglecting the presence of the magnetic current density vector \mathbf{M} , it is possible to write:

$$\nabla \times (\mathbf{E} + i\omega \mathbf{f}) = 0 \quad (2.5)$$

An important observation is that the rotor of the vector enclosed by circular brackets is null, so it is irrotational. As a consequence, it exists at least one potential scalar (ϕ) such as:

$$\exists | \phi : \quad \mathbf{E} + i\omega \mathbf{f} = -\nabla \phi \quad (2.6)$$

The way with which the expression of the potentials is derived is out of the scope of the thesis, but only the final result is shown. For more detailed information, see [11].

$$\begin{cases} \nabla^2 \mathbf{f} + k^2 \mathbf{f} = -\mu \mathbf{J} \\ \nabla^2 \phi + k^2 \phi = -\frac{\rho}{\epsilon} \\ \nabla \cdot \mathbf{f} + i\omega \epsilon \mu \phi = 0 \end{cases} \quad (2.7)$$

Where k is the propagation constant. The last equation of (2.7) is the so called Lorenz gauge. It is helpful to decouple the first two equations and to reduce the

degrees of freedom on the choice of the vector and scalar potentials. The most powerful property of the Lorenz gauge is that it is relativistic invariant, that is if it is valid for a certain reference frame, it is still valid for all the possible reference frames [12]. At this stage, once the the vector and scalar potential have been computed from (2.7) it is easy to get the electric field \mathbf{E} and the magnetic field \mathbf{H} . It is important to point out that if homogenous equations are considered, i.e. no external sources applied, it leads to a set of four scalar differential equations that have the same form.

If the homogenous equation of the vector potential is considered, so a free region space, a solution is given by: [13]

$$\mathbf{m} = \nabla f \times \mathbf{r} \quad (2.8)$$

$$\mathbf{n} = k^{-1} \nabla \times \mathbf{m} \quad (2.9)$$

The vector functions \mathbf{m} and \mathbf{n} can represent the vectors of electric and magnetic field in a medium that has the characteristic mentioned above. Concerning on a spherical reference frame, the analytical expressions of the fields are: [13]

$$\mathbf{E}(\mathbf{r}, \boldsymbol{\theta}, \phi) = \frac{k}{\sqrt{\mu}} \sum_{c,s,m,n} Q_{smn}^{(c)} \mathbf{F}_{smn}^{(c)}(\mathbf{r}, \boldsymbol{\theta}, \phi) \quad (2.10)$$

$$\mathbf{H}(\mathbf{r}, \boldsymbol{\theta}, \phi) = -ik\sqrt{\mu} \sum_{c,s,m,n} Q_{smn}^{(c)} \mathbf{F}_{3-smn}^{(c)}(\mathbf{r}, \boldsymbol{\theta}, \phi) \quad (2.11)$$

The complete expression of $\mathbf{F}_{smn}^{(c)}$ and $Q_{smn}^{(c)}$ can be found in the literature [13]. The former quantity is the expression of the waves functions while the latter quantity represents the wave coefficients.

The apex c indicates the property of the waves. With the choice of $c=1$ and $c=2$ we are refereeing to standing waves; choosing $c=3$ we are refereeing to an outward travelling wave, while $c=4$ to an inward travelling wave.

The subscripts $n=1,2,\dots$ and $m=0,1,\dots$ are used to generate the \mathbf{m} and \mathbf{n} functions. The subscript s is used to have a more compact notation. With $s=1$ we are refereeing to the \mathbf{m} function, while $s=2$ to the \mathbf{n} function.

Obviously, in the practice, the summation cannot be calculated for all the values, but it is truncated after some terms. The maximum terms of n and m are respectively N and M with the constraint $M \leq N$.

A more compact notation can be performed using the index $J = 2N(N+2)$. With this choice, as a result only one single summation is present instead of three [13].

$$\sum_{s=1}^2 \sum_{n=1}^N \sum_{m=-n}^M = \sum_{j=1}^J \quad (2.12)$$

The choice of the index N it is not so arbitrary. It depends essentially from the propagation constant k and from the radius of the minimum sphere r_0 , that is the smallest sphere possible able to subscribe the antenna. In general, a good choice of N is given by [13].

$$N = [kr_0] + n_1 \quad (2.13)$$

where the parameter n_1 depends on the required accuracy. At this stage, by a proper choice of N , it is possible to split the space into three regions:

- $r_0 \leq r \leq \frac{N}{k}$
- $\frac{N}{k} \leq r \leq \frac{4N^2}{\pi k}$
- $\frac{4N^2}{\pi k} \leq r < \infty$

The first one is called evanescent region, where the electromagnetic field does not propagate as a wave and the relationship between \mathbf{E} and \mathbf{H} is often complicated to predict [14]. One of the main characteristic is that the net energy that flows the region is equal to zero.

The second is the Fresnel region, or the so called near field region. With the hypothesis that the propagation is obtained by means of electric sources, the electric field has a dependence of $\frac{1}{r^2}$ while the magnetic field $\frac{1}{r^3}$. The situation is dual if the fields are generated by magnetic sources.

Another important property of the near field region comes out considering a power balance. The real part, i.e. the active power, is independent from r and it represents the power radiated by the sources; the imaginary part, i.e. the reactive power, has a dependence of $\frac{1}{r^3}$. As a result, the reactive power is confined in a region very close to the radiating source. The more the distance r is small, the worse the sources radiates [2]. Furthermore, in a region very close to the source, since the reactive power predominates over the active power, the measurements can be undetermined or ambiguous.

The last region is the Fraunhofer region, or the so called far field region. In this region, both for electric field and magnetic field the dependence is $\frac{1}{r}$.

In the practice, there is not a clear transition between the near field region and the far field region, but it is always present a transition zone where all the components of the fields must be taken into account.

In this thesis, in order to reconstruct the electromagnetic field scattered by the array of antennae, the measurements will be carried out in the near field region.

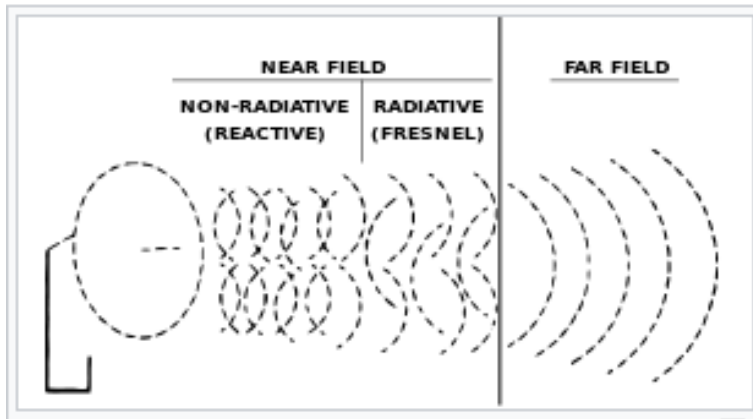


Figure 2.3. How the waves propagates in the 3 different regions. Credits to physics.stackexchange.com

2.3 ANTENNA UNDER TEST

In the thesis the antenna under test is a helix antenna, see Figure 2.4 .A helix antenna can be realized by a conducting wire wrapped on a cylindrical surface. Sometimes, the surface can be even filled with an insulating material, but this case won't be consider here.

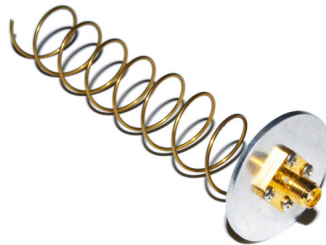


Figure 2.4. Picture of a helix antenna

The characteristics of the antenna are listed in Table 2.1 :

Parameter [symbol]	Value [unit of measure]
Frequency [f]	203 [MHz]
Wavelength [λ]	1.48 [m]
Propagation constant [k_0]	4.25 [m^{-1}]
Wave impedance [η_0]	377 [Ω]
Length x axis [x_{length}]	0.64 [m]
Length y axis [y_{length}]	0.64 [m]
Length z axis [z_{length}]	2.08 [m]
Distance x axis [x_{dist}]	0.74 [m]
Distance y axis [y_{dist}]	0.74 [m]

Table 2.1. Error computed as (5.4) for different cases, length trajectory 140m

The values of x_{dist} and y_{dist} refer to the spacing on the x and y axis of two consecutive antennae, in the case an array it is considered. This distance is computed from the centre of the first antenna with the centre of the successive one. The value of 0.74m corresponds to half wavelength. In this thesis will be considered the case of a single helix antenna and different arrays: 2x2, 3x3, 4x4.

In the case of a regular surface measurement that can be represented by a matrix, the surface spans from -8λ to $+8\lambda$ both on the x and y axis, with the origin of the coordinate system coincident with the centre of the helix antenna, in the case of a single one, or with the centre of the array.

The matrix is divided into smaller squares depending on the sampling; in particular, in the thesis a $\lambda/5$ and a $\lambda/10$ samplings are considered. A $\lambda/5$ sampling means that each wavelength 5 samples of the near field are taken; similar situation happens with a $\lambda/10$ sampling where 10 samples are taken. As a result, in the former case the resultant matrix has a size of 80x80 while in the latter case a size of 160x160.

For all the cases, the abscissa z for the measurement has kept constant for a value of 5λ (7.38m); obviously this is a simplification of a real situation, since it is impossible to flight a constant height with a drone.

For all the points of the matrix, that represents a certain Cartesian position in a (x,y,z) reference frame, with the origin of the reference frame mentioned above, it is simulated the near field radiated by the antenna under test in Matlab, without considering any disturbance. In the chapter 3 and 4 the simulated electromagnetic field can be described as a function: $\mathbf{E}(x, y) = \mathbf{E}_x(x, y) + \mathbf{E}_y(x, y)$. In the 5 chapter even the z component $\mathbf{E}_z(x, y)$ will be considered.

The antenna under test and the simulated near field, in the case of a $\lambda/5$ sampling, is shown in the following figures.

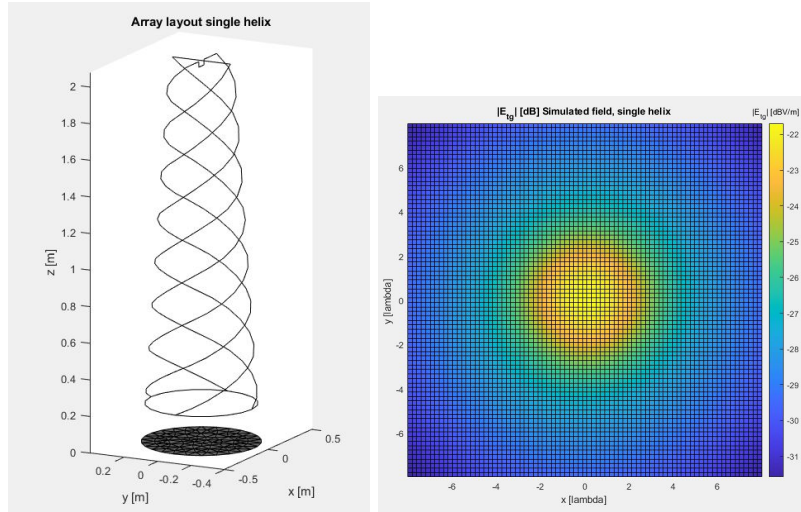


Figure 2.5. Single antenna layout and simulated field

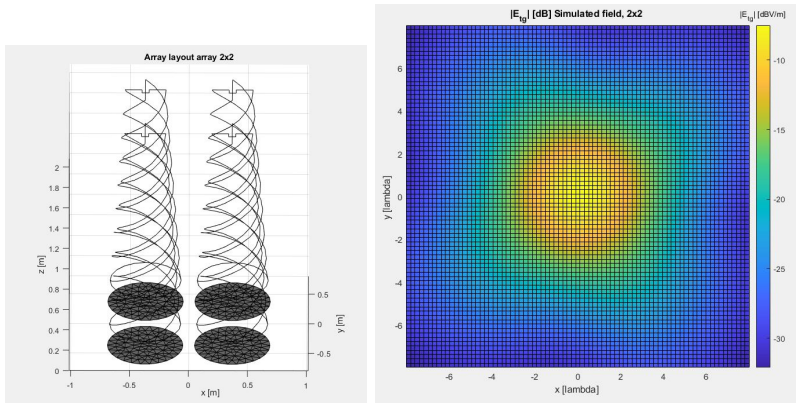


Figure 2.6. Array 2x2 layout and simulated field

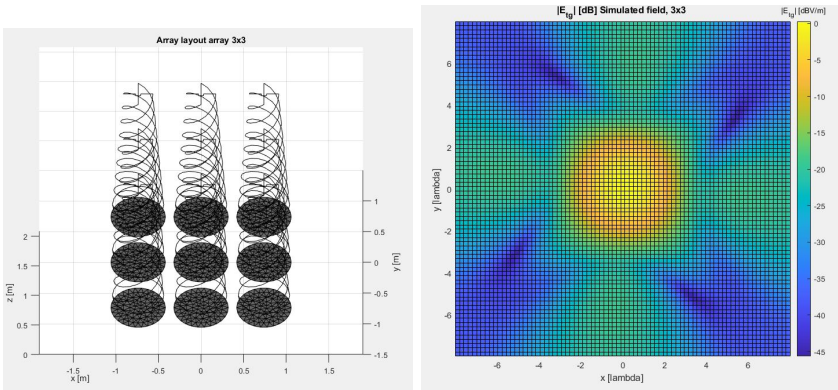


Figure 2.7. Array 3x3 layout and simulated field

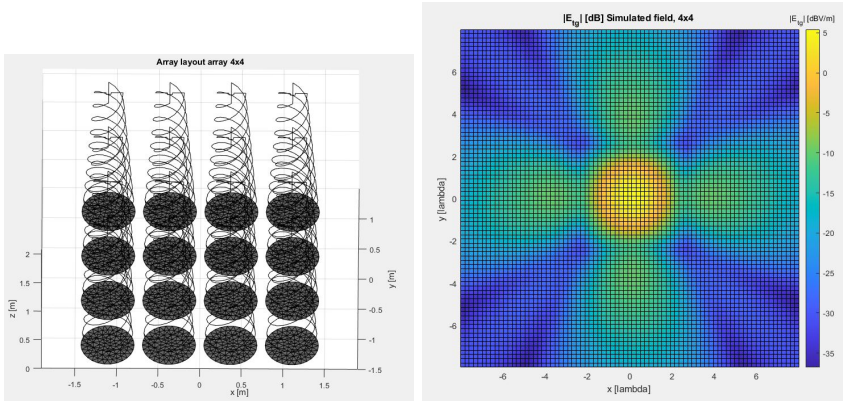


Figure 2.8. Array 4x4 layout and simulated field

The figures shows the plot of the simulated value in Decibel computed as:

$$20 * \log_{10} \sqrt{|\mathbf{E}_x(x, y)|^2 + |\mathbf{E}_y(x, y)|^2} \quad (2.14)$$

As it is possible to notice from the figures, by increasing the number of antennae, it increases the gain in the central region, put in correspondence of the origin of the reference frame. In a few words, by increasing the number of elements of the array, the complexity of the electromagnetic field increases, since the gain in the region with the highest directivity increases. This is translated into a bigger error on the reconstruction of the field when an array 4x4 is considered rather than the case when the scattering object is composed by a single helix antenna.

Chapter 3

CVX SOFTWARE

The main goal of the thesis is to reconstruct the electromagnetic field scattered by an array of antennae, using only a few entries and without having any a priori knowledge about the transmitting system; using this starting scenario, the reconstruction of the electromagnetic field does not match perfectly the scattered field, since an error is always present due to the fact that the available information are not enough to perfectly reconstruct the field.

In this chapter will be described an algorithm used in order to achieve the matrix reconstruction representing the scattered field. The algorithm used is described in the article [15]. It is applied on different sources and it uses only a limited number of data, selected randomly. It can be applied for any sources, without any requirements on priori information of the source itself. The algorithm is obtained by mixing together two regularizers: the thin plate spline interpolation (TPS) and the interpolation by the minimization of the nuclear norm. In the following, both procedures are explained.

3.1 THIN PLATE SPLINE

A spline is a mathematical function used to interpolate a set of points in a generic interval. A requirement to satisfy is that the interpolated function is continuous until a certain order for all the points of the set. The thin plate spline (TPS) is a polyharmonic spline introduced by Duchon in the last century. The interpolation function belongs to the class C^1 , i.e. it has continuous first partial derivatives. The objective function of the TPS interpolation is to minimize an energy function. Considering a 2D problem, assuming that f is a function that goes from R^2 to R with square integrable second derivatives, assuming a finite set of points in R^2 that are all different and not collinear, $\Upsilon = \{\mathbf{v}_i : i = 1, 2, \dots, n\}$, then the thin plate spline interpolant f on Υ is a function that minimizes the integral: [16]

$$I(s) = \int_{R^2} \left(\frac{\partial^2 s}{\partial \zeta^2} \right)^2 + 2 \left(\frac{\partial^2 s}{\partial \zeta \partial \eta} \right)^2 + \left(\frac{\partial^2 s}{\partial \eta^2} \right)^2 dx dy \quad (3.1)$$

with the constraint that:

$$s(v_i) = f(v_i), \quad i = 1, 2, \dots, n \quad (3.2)$$

where in the equation (3.1) the symbols ζ and η indicate two generic components of the vector \mathbf{x} .

The TPS method is highly used because it can be found a closed form solution by

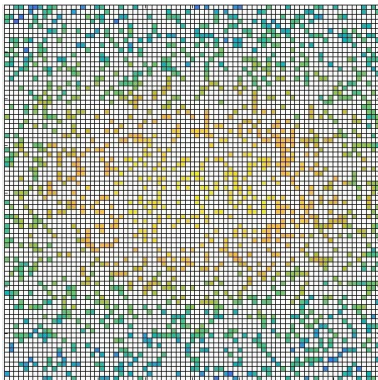


Figure 3.1. Example of an uniform lattice Ω , 80×80 , where 1600 samples are randomly selected.

solving a linear system and then the set of points of Υ can be in general positions. Let assume to have a generic radiating source and let assume that the radiated electromagnetic field on a given uniform lattice Ω has dimensions of m by n . The fundamental assumption is that the field is not measured in all the points of the lattice Ω but only in a set of random positions p , where $p < m \cdot n$, as in Figure 3.1. At this stage, the thin plate interpolation $f(\mathbf{r})$ can be seen as a superimposition of radial basis functions $\Phi(\mathbf{r})$ computed in all the points where the field is measured, weighted with coefficients c_i . [15]

$$f(\mathbf{r}) = \sum_{i=1}^p c_i \Phi(|r - r_i|) \quad (3.3)$$

The basis functions $\Phi(\mathbf{r})$ are computed as: [15]

$$\Phi(\mathbf{r}) = -r^2 \log(r^2) \quad (3.4)$$

with the assumption that $r = \sqrt{x^2 + y^2}$. The weighted coefficients of the equation (3.3) can be computed by the knowledge of the electromagnetic field computed at position \mathbf{r}_k . [15]

For those points who are not measured but interpolated by TPS algorithm, i.e. for all the points $i = 1, \dots, (m \cdot n) - p$, at the position \mathbf{r}_i , the value is given by $\check{e}_i = f(\mathbf{r}_i)$.

3.2 NUCLEAR NORM MINIMIZATION

The problem of the reconstruction of the matrix can be seen as a problem of matrix completion, where the aim is to find the values of a generic $m \cdot n$ matrix, denoted with \mathbf{M} , given a sparse set of observation Ω . An important assumption is that the matrix \mathbf{M} is a low-rank matrix.

This can be solved by means of the rank minimization problem. The objective function of the rank minimization problem is given by:

$$\text{minimize} \quad \text{rank}(\mathbf{X}) \tag{3.5}$$

and subjected to the constraint:

$$\text{s.t.} \quad \mathbf{X}_{ij} = \mathbf{M}_{ij} \quad \text{where } (i, j) \in \Omega \tag{3.6}$$

where \mathbf{X} is a decision variable and $\text{rank}(\mathbf{X})$ is equal to the rank of the matrix to be reconstructed \mathbf{M} .

Unfortunately, the relation (3.5) can not be used in the practice since it is a non-deterministic polynomial time hardness problem; as a consequence, the time in order to find the solution depends doubly exponentially in the dimension n of the matrix.[17]

A convex optimization problem can be found by relaxing the objective function (3.5) by replacing the $\text{rank}(\mathbf{X})$ with its nuclear norm $\|\mathbf{X}\|_*$ [18]. It becomes:

$$\text{minimize} \quad \|\mathbf{X}\|_* \tag{3.7}$$

where the nuclear norm $\|\mathbf{X}\|_*$ has defined as:

$$\|\mathbf{X}\|_* = \text{trace}(\sqrt{\mathbf{X}\mathbf{X}^t}) = \sum_k \sigma_k \tag{3.8}$$

where σ_k indicate the singular values of the matrix \mathbf{X} .

A further modification of the objective function (3.7) can be done by expressing the nuclear norm in a positive semi-definite form [19]. In this way the objective function becomes:

$$\text{minimize} \quad \text{trace}(\mathbf{Y}) + \text{trace}(\mathbf{Z}) \tag{3.9}$$

where in addition to the constraint given in (3.6), the (3.9) is subjected to:

$$\begin{bmatrix} \mathbf{Y} & \mathbf{X} \\ \mathbf{X}^t & \mathbf{Z} \end{bmatrix} \geq 0 \tag{3.10}$$

where the matrix \mathbf{Y} and \mathbf{Z} are Hermitian matrices and their dimensions are respectively $m \cdot m$ and $n \cdot n$. By solving this problem the simplest representation suitable with the available data is found, that corresponds to the simplest electromagnetic

source that is able to scatter the field described by \mathbf{M} .

3.3 ALGORITHM

The algorithm proposed in [15] combines the techniques of the thin plate spline and the nuclear norm minimization in order to obtain a reconstruction of a matrix \mathbf{M} , dimension $m \cdot n$, representing the electromagnetic field radiated by a source, where only p , with $p < m \cdot n$, samples are measured and they are collected in the vector \mathbf{e} .

The combination of the two techniques is useful because with the TSP, solving the (3.9), a significant underestimation of the field appears when a sequence of adjacent data is missing [15]. The interpolated field using TPS is collected in a vector $\check{\mathbf{e}}$.

By mixing together (3.3),(3.4) and (3.9), subjected to the constraints given by (3.6) and (3.10) the objective function of the algorithm is [15]:

$$\min_{\mathbf{X} \in C^{m \cdot n}} \|\mathbf{X}\|_* + \alpha \|\mathbf{W}(A^c(\mathbf{X}) - \check{\mathbf{e}})\|_2 \quad (3.11)$$

subject to:

$$\|A(\mathbf{X}) - \mathbf{e}\|_2 \leq \epsilon \quad (3.12)$$

The operator $A(\mathbf{X})$ is the linear map: it selects only the p measured samples from the uniform lattice Ω . Its complementary is given by $A^c(\mathbf{X})$ that selects the $(m \cdot n - p)$ points that are not measured. The matrix \mathbf{W} is a diagonal matrix, where each entry is given by $W_{i,i} = |\check{\mathbf{e}}_i|^{-1}$. The threshold value ϵ takes into account the noise level that affects the measured data \mathbf{e} . The parameter α is

called the regularization parameter; it indicates how the algorithm relies on the minimization of the nuclear norm and how it relies on the interpolation through TPS. It is positive definite, i.e. $\alpha \in (0, +\infty)$

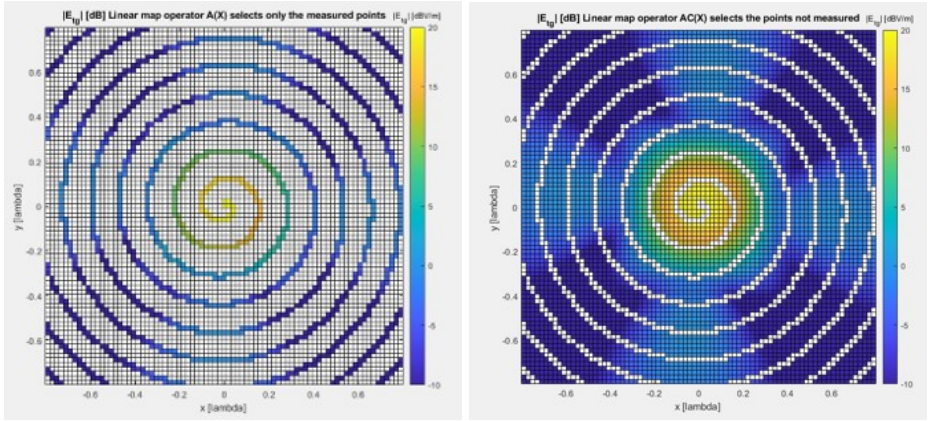


Figure 3.2. Example of how the linear map and its complementary work

3.4 PATH OF THE DRONE

A very important difference with respect to the procedure described in the [15] regards how the samples are measured.

The goal is to measure the electromagnetic field on a surface by using a drone. For this reason, the samples are not chosen randomly but according to various trajectories that are able to represent qualitatively a 2D flight of a drone, where, in this case, the z abscissa is supposed to be constant.

In particular, three different trajectories have been analysed.

- RADIAL FLIGHT

The function used in order to simulate a radial flight for the drone can be roughly described as a superimposition of straight lines, with different slopes with respect to the horizontal axis.

$$\sum_{i=1}^n y(x) = i * \theta_0 * x \quad (3.13)$$

where the initial angle θ_0 is chosen by the user in range so that $\theta_0 \in [15; 30; 45; 60; 90]^\circ$, while the final term of the sum n is given by $n = (\frac{180}{\theta_0} - 1)$. An example is given in figure 3.3.

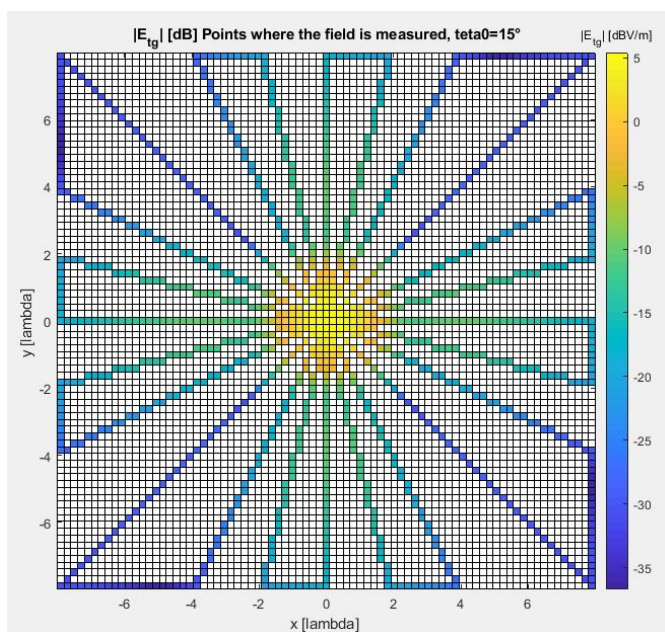


Figure 3.3. Example of radial pattern where $\theta_0=15^\circ$

- SPIRAL FLIGHT

The function used in order to simulate approximately a spiral flight is of the

type:

$$\begin{cases} X(\epsilon) = A * \epsilon * \cos(\omega\epsilon) \\ Y(\epsilon) = A * \epsilon * \sin(\omega\epsilon) \end{cases} \quad (3.14)$$

where A is the amplitude of the spiral function, ϵ is the independent variable that represents the x and y coordinates, while ω represents is a spatial frequency. The parameters tuned by the user are A and ω . By their tuning, different shapes of the spiral are considered, and consequently different numbers of samples where the electromagnetic field is measured. An example is given in the figure 3.4.

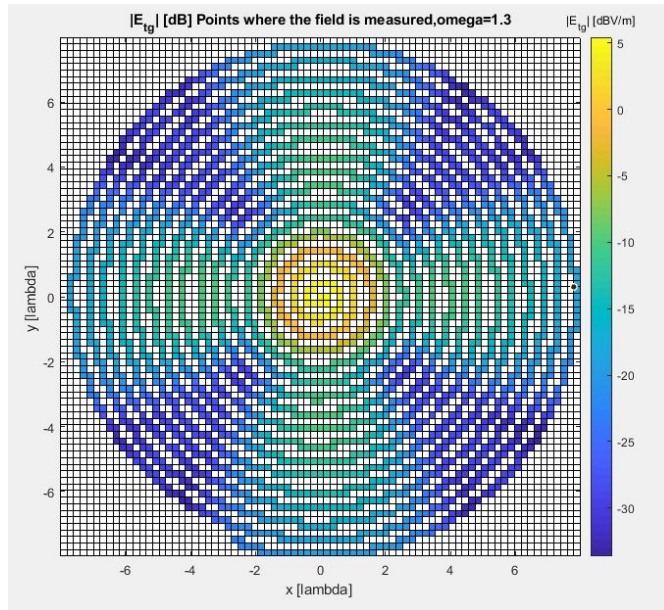


Figure 3.4. Example of spiral pattern, where $A=0.1$ and $\omega=1.3$

- RECTANGULAR PULSE FLIGHT The function used in order to describe

the flight of the drone is a train of rectangular pulses. The amplitude of the rect is chosen by the user. An example is given in the figure 3.4.

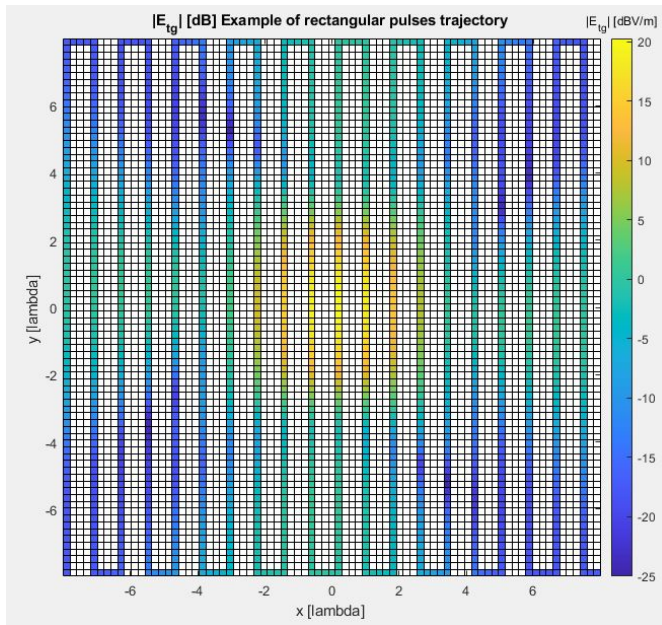


Figure 3.5. Example of a rectangular pulse flight

3.5 SIMULATION AND ANALYSIS

The equation (3.11) with the constraint given by (3.12) have been implemented on Matlab. Unlike the case of the paper [15], where the matrix \mathbf{W} has been chosen as a diagonal matrix and each entry given by $W_{i,i} = |\check{\mathbf{e}}_i|^{-1}$, in the thesis \mathbf{W} has been chosen as a diagonal matrix where each entry has been set equal to 1. The threshold value, ϵ , has been chosen empirically equal to 10^{-6} . This value is so small because the electromagnetic field radiated by the array has been simulated through Matlab, so no noise affects the measurements.

The algorithm implemented on Matlab can be subdivided into four steps:

- i. The first step is to simulate the electromagnetic field scattered by the array, and load on Matlab as a matrix, of dimension $m \cdot n$. Each entry of the matrix represents the value of the field in a point of a Cartesian reference frame;
- ii. The second step is to select the p points where the field has been measured by means of one of the trajectory shown in Section 3.4;
- iii. Once that the trajectory has been selected and ,consequently, the points where the field is measured, starting from these points the algorithm interpolates by means of the spline the field in the remaining $(m \cdot n) - p$ points.
- iv. The final step is to minimize the rank of the unknown matrix starting from the measured values and the interpolated values find in the previous step. The minimization of the rank has done thought CVX software; the minimization has been carried out separately for the real and imaginary part of the x and y components.

In order to evaluate the performance of the algorithm, two kinds of errors are considered. The first is computed as:

$$\frac{\sqrt{\text{norm}(\mathbf{E}\mathbf{x} - \mathbf{E}\mathbf{x}_{spline})^2 + \text{norm}(\mathbf{E}\mathbf{y} - \mathbf{E}\mathbf{y}_{spline})^2}}{\sqrt{\text{norm}(\mathbf{E}\mathbf{x})^2 + \text{norm}(\mathbf{E}\mathbf{y})^2}} \quad (3.15)$$

$$\frac{\sqrt{\text{norm}(\mathbf{E}\mathbf{x} - \mathbf{E}\mathbf{x}_{cvx})^2 + \text{norm}(\mathbf{E}\mathbf{y} - \mathbf{E}\mathbf{y}_{cvx})^2}}{\sqrt{\text{norm}(\mathbf{E}\mathbf{x})^2 + \text{norm}(\mathbf{E}\mathbf{y})^2}} \quad (3.16)$$

The second manner is basically the same, but instead of computed the norm of the matrices by means of the Matlab command "norm", it has been computed

using the Frobenius norm. The command "norm(X)", where X is a generic matrix, returns the maximum singular value of the matrix X, that for a first approximation it is the maximum of $\text{svd}(X)$. Instead, the Frobenius norm of a generic matrix X has defined as: $\|X\|_F = \sqrt{\text{trace}(X^t X)}$.

In the equations (3.15) and (3.16) the matrices \mathbf{Ex} and \mathbf{Ey} represent the matrix where the values of the x and y component of the simulated electromagnetic field are stored; in (3.15) the matrices \mathbf{Ex}_{spline} and \mathbf{Ey}_{spline} are the x and y components of the field interpolated using the spline; in (3.16) the matrices \mathbf{Ex}_{cvx} and \mathbf{Ey}_{cvx} are the x and y components of the field after the minimization of the nuclear norm. Since that in this section a $\lambda/5$ sampling is performed, the unknown matrix to be reconstructed has dimension 80×80 , so in total there are 6400 points that represents the electromagnetic field in the space.

In the following the obtained results are shown in the case of a 3×3 array.

3.5.1 RESULTS RADIAL PATH CVX

In this first step, the regularization parameter α has be set equal to 1, while it has been changed the initial angle θ_0 of the radial function. In this case only the error computed as (3.16) and (3.15) has been taken into account; furthermore, no error on the trajectory of the drone is considered. The results are shown in the table 3.1 :

As it is possible to notice, the best case is when $\theta_0 = 15^\circ$, that corresponds an amount of 1055 points where the field is measured, while in the remaining 5345 points the field is first interpolated by the spline and then the CVX software minimize the nuclear norm of the resulting matrix. The second column of the table 3.1 refers in the case when only the interpolation with the spline is carried

Angle θ_0 [°]	Error splines [%]	Error splines+CVX [%]
90	119	80.0
60	41.2	48.2
45	29.1	35.1
30	23.3	26.3
15	13.4	11.1

Table 3.1. Variation of the error with respect to θ_0 , radial trajectory, CVX

out, while the third column when both spline and CVX software are used. In the case $\theta_0 = 15^\circ$ the total length of the flight of the drone is approximately equal to 180m.

At this stage, it has been changed the parameter α when $\theta_0 = 15^\circ$, in order to find the range of values that give the best results.

α	Error splines+CVX [%]
0.01	10.5
0.1	10.2
1	11.1
3	12.4
5	13.0

Table 3.2. Variation of the error with respect to α , when $\theta_0 = 15^\circ$

The best result is achieved when $\alpha=0.1$. By increasing α the algorithm relies more on the interpolation through the spline rather than the minimization of the nuclear norm, for this reason by increasing the order of magnitude of α the error when using both spline and CVX is pretty close to the case when only spline is used. In the case $\alpha = 0.1$, that corresponds to the best case, the Frobenius norm of the error when both spline and CVX software is considered is equal to 13.6%, while in the case only the spline is used the error is equal to 20.2%.

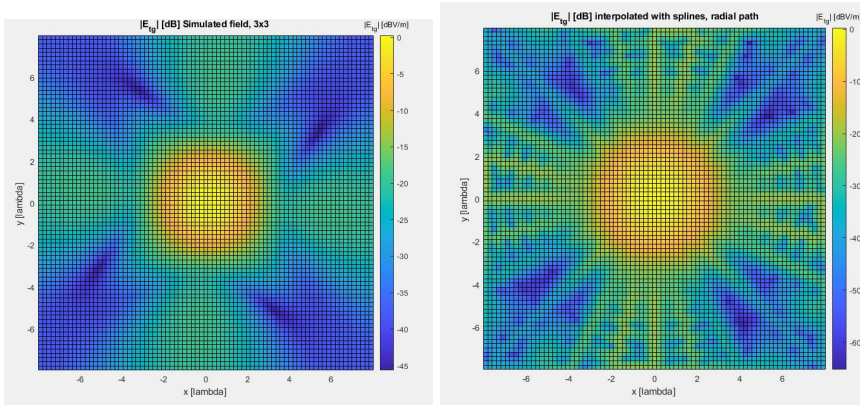


Figure 3.6. Difference between the simulated and the interpolated field.
 $\theta_0 = 15^\circ$, radial path

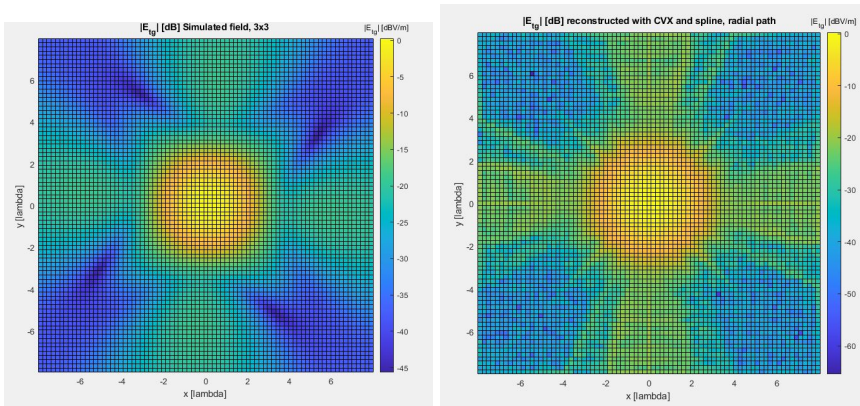


Figure 3.7. Difference between the simulated and the interpolated field.
 $\alpha = 0.1$, radial path

At this stage an error on the trajectory of the drone is considered; the error is obtained through a random variable: in particular, naming the value of the random variable in a point that represents the trajectory of the drone as j_i , if $0 < j_i \leq 0.2$ the i point is moved upward, if $0.2 < j_i \leq 0.4$ the i point is moved downward, while

if $0.4 < ji \leq 1$ the i point remains in its position. The index i is that $i = 1, \dots, N$ where N is the number of points where the electromagnetic field is measured, i.e. when $\theta_0 = 15^\circ N = 1055$. A number of 20 simulations have been carried out and the error computed through (3.16) is equal to 10.2 ± 0.6 .

3.5.2 RESULT SPIRAL PATH CVX

As in 3.5.1, the parameter α has be kept equal to 1. It has been kept constant while the parameter ω of the spiral pattern has been varied; no error on the trajectory of the drone is assumed. The results are shown in the table 3.3 :

ω	Error splines [%]	Error splines + CVX [%]
0.5	43.3	42.7
0.8	24.8	24.5
1.1	16.9	15.1

Table 3.3. Variation of the error with respect to ω , spiral trajectory CVX

In this case, the number of points able to achieve an error of 15.1% are around the 30% of all the points of the matrix. This is a worse results with respect to the case of the radial trajectory.

The successive step was to kept $\omega = 1.1$ and changes the value of α . The results are shown in Table 3.4:

α	Error splines + CVX [%]
0.1	17.2
1	15.1
3	15.4
5	16.3

Table 3.4. Variation of the error with respect to α , spiral trajectory, $\omega = 1.1$

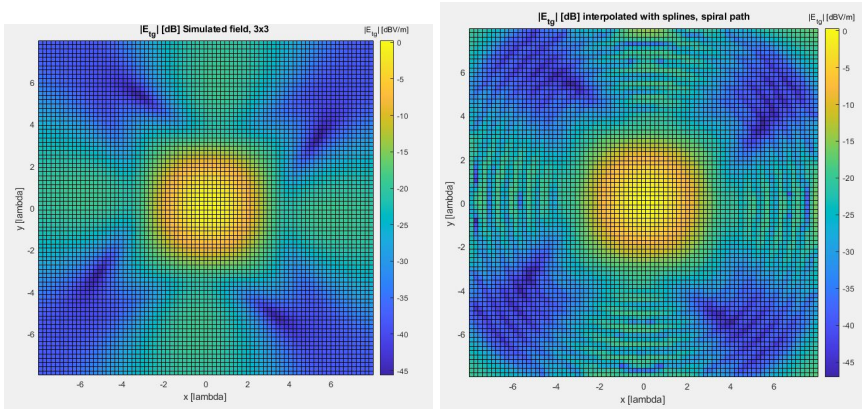


Figure 3.8. Difference between the simulated and the interpolated field.
 $\omega = 1.1$, spiral path

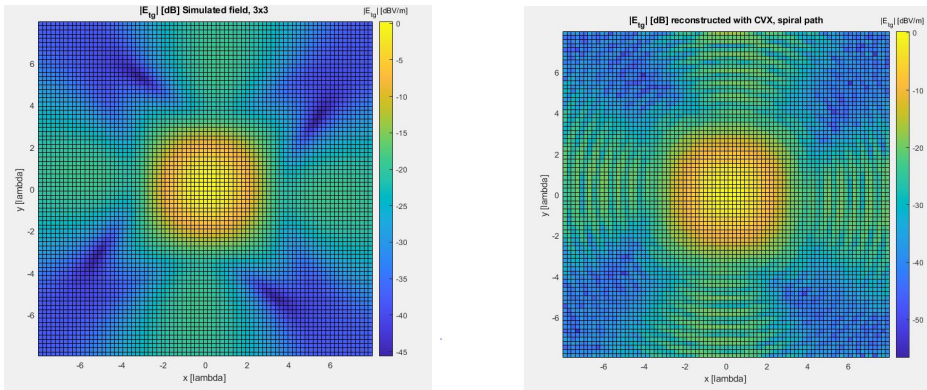


Figure 3.9. Difference between the simulated and reconstructed field. $\omega = 1.1$ $\alpha = 1$, spiral path

A further increment of α would be useless since the algorithm would rely more on the interpolation through the splines but, in this case, the error achieved with the splines is higher than in the case when even the minimization of the nuclear norm is used.

At this point it has been considered an error of the trajectory of the pattern as described in 3.5.1. The error is obtained averaging out 20 simulations and it is equal to 15.2 ± 0.1 .

3.5.3 RESULT RECTANGULAR PULSE FLIGHT CVX

As in the previous the parameter α was kept equal to 1 and in this case has been changed the amplitude of the rect. The results are shown in the table :

Amplitude	Error splines [%]	Error splines + CVX [%]
3	25.6	54.8
4	29.7	64.6
5	33.2	69.7
6	45.2	74.5

Table 3.5. Variation of the error with respect to the amplitude, rectangular pulses flight

The best case is when the amplitude is equal to 3. Again, another table is shown, where this time change the parameter α .

α	Error splines + CVX [%]
0.1	78.3
1	54.8
3	25.7
5	25.5
10	25.5

Table 3.6. Variation of the error with respect to α , amplitude =3, rectangular pulses flight

Taking into account that the amount of samples to achieve an error of 25.5% is quite big, around the 50% of measured points, in the following chapter no simulations

on a rectangular pulse flight will be carried out.

Chapter 4

SINGULAR VALUE THRESHOLDING

The method used for the reconstruction of the electromagnetic field cited in the article [15] and described in the previous chapter is a powerful method but it has some drawbacks.

To minimize the objective function in (3.7) the CVX software is used. Its main limit is due to the computational time for the computation of the minimization of the nuclear norm.

In Chapter 3, the algorithm in (3.11) has been tested for an unknown matrix of a size $80 \cdot 80$, so for an amount of 6400 points that describe the simulated electromagnetic field of the array. But, the final goal is to manage matrices that can describe a realistic problem, for example by performing a $\lambda/10$ sampling. Therefore, there is the necessity to work with matrices with bigger sizes. For this reason, the CVX software can not be used in practice because the computational time for getting

the result would be not acceptable. Moreover, the obtained error is not negligible, so it was necessary to exploit a new solution.

In this chapter it is described another algorithm that performs the minimization of the nuclear norm: the singular value threshold (SVT) algorithm. Both the cases of a $\lambda/10$ sampling and a $\lambda/5$ sampling here are presented.

4.1 THE ALGORITHM

Let's consider a generic \mathbf{A} matrix of size $n \cdot m$. The matrix can be decomposed as:

$$\mathbf{A} = \mathbf{U}\mathbf{\Sigma}\mathbf{V}^* \tag{4.1}$$

where the matrix $\mathbf{\Sigma}$ is a diagonal matrix so that $\mathbf{\Sigma} = \text{diag}(\sigma_i), i = 1, \dots, r$; r is the rank of the matrix \mathbf{A} , σ_i are the singular value. For each $\tau \geq 0$ it possible to introduce an operator such that [20]:

$$D_\tau(\mathbf{A}) := \mathbf{U}D_\tau(\mathbf{\Sigma})\mathbf{V}^* \tag{4.2}$$

where the function $D_\tau(\mathbf{\Sigma})$ is defined as:

$$D_\tau(\mathbf{\Sigma}) = \text{diag}(\{(\sigma_i - \tau)_+\}) \tag{4.3}$$

The operator in (4.3) is the so called singular value shrinkage operator. With the notation $(\sigma_i - \tau)_+$ only the positive is considered, such that: $(\sigma_i - \tau)_+ = \max(0, (\sigma_i - \tau))$. If there are several σ_i that are below the threshold τ the consequence

is that $\text{rank}(D_\tau(\Sigma)) \ll \text{rank}(\mathbf{A})$.

Now, let's consider that \mathbf{M} is the unknown matrix that has to be reconstructed, of size $m \cdot n$ where only p , with $p < m \cdot n$, points are observed, $p \in \Omega^{n^1 \cdot n^2}$. Assuming that $\tau > 0$, a sequence δ_k of positive step sizes, \mathbf{X} is the matrix reconstructed and considering a starting \mathbf{Y}_0 , it is possible to define an iterative procedure such that [20]:

$$\begin{cases} \mathbf{X}^k = D_\tau(\mathbf{Y}^{(k-1)}) \\ \mathbf{Y}^k = \mathbf{Y}^{(k-1)} + \delta_k P_\Omega(\mathbf{M} - \mathbf{X}^k) \end{cases} \quad (4.4)$$

The equation (4.4) stops when a stopping criteria is reached. The sequence of \mathbf{X}^k converges to this solution [20]:

$$\text{minimize} \quad \tau \|\mathbf{X}\|_* + \frac{1}{2} \|\mathbf{X}\|_F^2 \quad (4.5)$$

The constraints of the objective function are the same of the equation (3.6).

$$\text{s.t.} \quad \mathbf{X}_{ij} = \mathbf{M}_{ij} \quad \text{where } (i, j) \in \Omega \quad (4.6)$$

In the equation (4.5) the second term is the square of the Frobenius norm of the matrix \mathbf{X} . It is easy to notice that if τ is sufficiently big the (4.5) tends to (3.7).

In this thesis, the used algorithm to perform the SVT decomposition has been developed by Candès et al, and it can be found in [17]. The user has to set some parameters as input for the algorithm:

- The parameter τ . Referring to 4.5 bigger is the value of τ , the more (4.5) tends to (3.7); its implies that the objective function relies more on the

minimization of the nuclear norm rather on the minimization of the Frobenius norm. According to [17], a good choice is to set $\tau = \sqrt{m \cdot n}$, where m and n are the sizes of the unknown matrix \mathbf{M} ;

- The step size δ . The convergence of the problem is guaranteed if $0 < \delta < 2$; anyway, this choice of δ sometimes is too conservative and the convergence is slow. Here, it has been simulated even cases when $\delta > 2$;
- The stopping criteria ϵ . It indicates that the algorithm stops when $\frac{\|P_{\Omega}(\mathbf{X}^K - \mathbf{M})\|_F}{\|P_{\Omega}(\mathbf{M})\|_F} < \epsilon$; a suggested stopping criteria is to set $\epsilon = 10^{-4}$;
- The maximum number of iteration before the algorithm stops. In this thesis, it has been set equal to 750.

In order to evaluate the performance of the algorithm, two kinds of error are considered:

$$\frac{\sqrt{\text{norm}(\mathbf{E}_x - \mathbf{E}_{x,svt})^2 + \text{norm}(\mathbf{E}_y - \mathbf{E}_{y,svt})^2}}{\sqrt{\text{norm}(\mathbf{E}_x)^2 + \text{norm}(\mathbf{E}_y)^2}} \quad (4.7)$$

$$\frac{\sqrt{\text{frob}(\mathbf{E}_x - \mathbf{E}_{x,svt})^2 + \text{frob}(\mathbf{E}_y - \mathbf{E}_{y,svt})^2}}{\sqrt{\text{frob}(\mathbf{E}_x)^2 + \text{frob}(\mathbf{E}_y)^2}} \quad (4.8)$$

In the formulae (4.7) and (4.8), the matrices \mathbf{E}_x and \mathbf{E}_y represent respectively the x and the y components of the original simulated field; the matrices $\mathbf{E}_{x,svt}$ and $\mathbf{E}_{y,svt}$ represent the respectively the x and the y components of the reconstructed field by the SVT algorithm.

The error (4.7) is computed by considering the l2 norm of the matrix. In Matlab, the command `norm(X)`, where X is a generic matrix, returns the maximum singular value of the matrix X; whereas, the error (4.8) is computed by considering the

frobenius norm of the matrix. The frobenius norm of a generic matrix X is given by: $frob(X) = \sqrt{trace(X^T X)}$.

4.2 RADIAL PATH SVT

Here we consider the case when the samples are taken accordingly to a radial path; the characteristics of the scattering object are the same of that presented in Section 2.3, with a $\lambda/10$ sampling. The trajectory of the radial flight has been introduced in Chapter 3 and an example is given by the figure 3.3.

The first step is to find the best values for the input parameters of the SVT algorithm; for this purpose, it has been considered a matrix surface that goes from -8λ to $+8\lambda$, with $\lambda = 1.48m$, it has considered a $\lambda/5$ sampling, and as a result the electromagnetic field is represented by a 80×80 square matrix. The initial angle, θ_0 , of the formula (3.13) has chosen such that: $\theta_0 = 15^\circ$. The number of the maximum iteration has set to 750 and the stopping criteria $\epsilon = 10^{-4}$. The obtained results are shown in the table 4.2, computed using the command norm, and in the table 4.1, computed using the Frobenius norm. The percentage error is computed according to (4.7) and (4.8). The test has done by considering a 4×4 array as in the figure 4.2.

As it is possible to see in the tables, the best cases are obtained when $\tau = 80$.

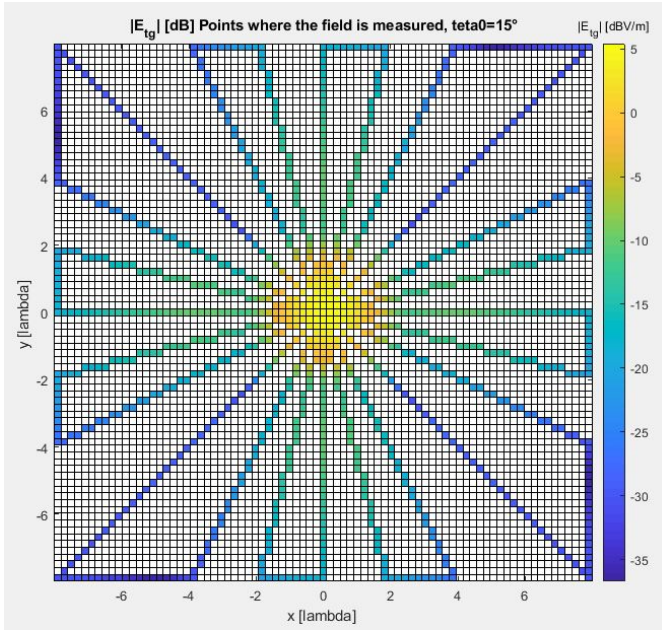


Figure 4.1. Measured points setting $\theta_0=15^\circ$

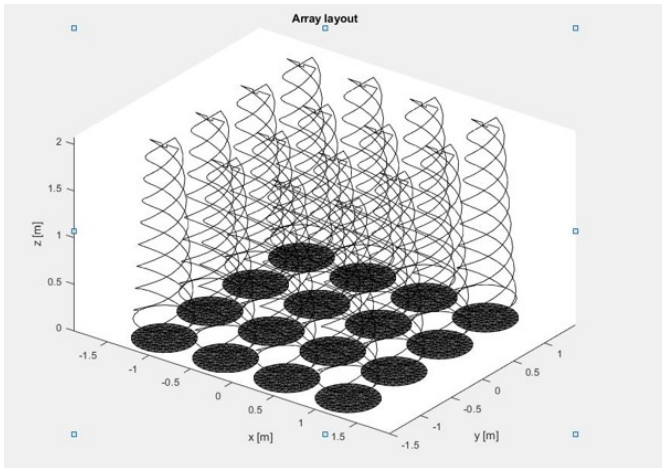


Figure 4.2. Layout of the array 4x4 of helix antennae

	δ	0.5	1	1.5	1.8	2.3	3
τ							
80		12.6	11.8	11.7	11.6	11.6	65.6
400		17.5	17.1	13.3	12.6	12.0	65.6
800		20.1	17.4	17.1	17.1	14.6	62.0
1600		26.1	20.1	18.1	17.6	11.3	17.1
3200		33.4	26.1	22.2	20.8	19.2	18.1
4800		37.2	30.4	26.0	24.2	22.0	17.5

Table 4.1. Variation of (4.8), [%], wrt τ and δ

	δ	0.5	1	1.5	1.8	2.3	3
τ							
80		7.91	7.56	7.57	7.50	7.54	65.1
400		14.9	7.73	7.73	8.77	7.92	65.2
800		17.2	14.5	14.5	14.5	11.5	61.3
1600		22.4	15.4	15.4	15.0	14.5	14.5
3200		29.1	22.3	18.9	17.7	16.4	15.4
4800		32.6	26.3	22.3	20.7	18.7	17.7

Table 4.2. Variation of (4.7), [%], wrt τ and δ

This value, together with the value of $\delta = 1.8$ are set for the successive simulations. In order to evaluate better the performance of this choice of τ and δ an error on the measurement has been introduced, as mentioned in the chapter 3. Running 10 simulations, it has been obtained:

Error (4.8) [%]	Error (4.7) [%]	Computational time [s]
8.49 ± 0.0190	7.51 ± 0.0106	6.18 ± 0.82

Table 4.3. Variation of the error considering an error, SVT, radial

Since the variance of the errors and of the computational time can be considered small, it is possible to fix constant for the radial path the choice of $\delta = 1.8$ and $\tau = \text{sqrt}(n \cdot n)$, indicating with n the size of the matrix to be reconstructed. Here is shown the reconstructed field, without considering the error.

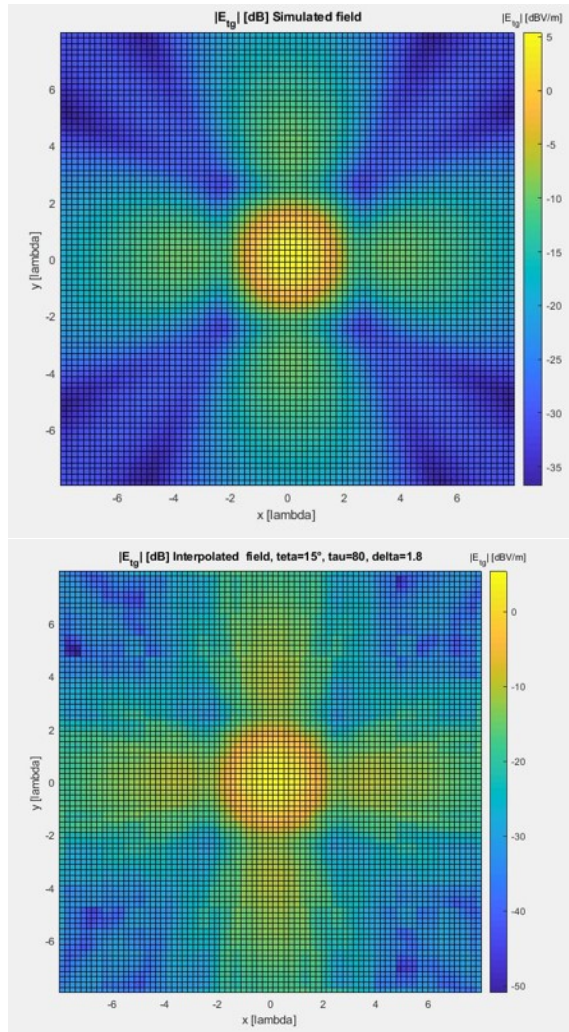


Figure 4.3. Reconstructed field with the SVT, 4×4 array, $\lambda/5$ sampling

Now, it will be considered the case when a $\lambda/10$ sampling is performed; in this case, the unknown matrix that has to be reconstructed has a size of 160×160 . With the previous choice of input parameters, now τ becomes $\tau = 160$. By considering a

layout as in the figure 4.2, several simulations have carried out, depending on the percentage of measured points. The results are listed in the table 4.4.

Percentage of measured points [%]	Error with frobenius norm, (4.7),[%]
5	43.9
10	25.1
15	15.6
20	8.62
25	4.50

Table 4.4. Variation of the error wrt percentage of measured points, svt, radial path

An example of the reconstructed field using the 20% of points is given in the figure 4.4. On the left there is the simulated field, while on the right there is the reconstructed one. The input parameters for the SVT algorithm was $\tau=160$ and $\delta=1.8$, while for the radial path the angle θ_0 was set equal to 15° .

4.3 SPIRAL PATH SVT

With all the starting hypothesis of the section 4.2, the same analysis is carried out in the case of spiral path. Referring to the formula (3.14), setting $A=0.15$ and $\omega = 1.3$, the tables 4.6, where the command norm is used, and the table 4.5, where instead the frobenius norm is used, are compiled.

As in the previous case, the best result is achieved by selecting $\tau = 80$ and $\delta = 1.8$.

	δ	0.5	1	1.5	1.8	2.3	3
τ							
80		9.39	7.56	7.56	7.12	9.06	16.5
400		21.8	13.8	11.8	10.3	11.3	18.0
800		24.4	21.7	15.1	14.1	14.9	11.7
1600		30.5	24.3	22.3	21.9	22.8	15.0
3200		30.8	30.4	26.5	25.8	25.9	22.3
4800		42.7	34.9	30.4	28.5	30.0	22.3

Table 4.5. Variation of (4.8), [%], wrt τ and δ , spiral path

	δ	0.5	1	1.5	1.8	2.3	3
τ							
80		7.21	6.26	6.19	6.14	7.02	15.9
400		16.1	9.09	8.24	7.66	8.66	16.2
800		17.3	16.1	9.26	9.26	10.1	18.9
1600		23.3	17.2	16.2	16.1	16.6	19.8
3200		31.8	23.3	19.1	17.8	18.6	16.2
4800		36.3	28.1	23.2	21.2	22.5	16.2

Table 4.6. Variation of (4.7), [%], wrt τ and δ , spiral path

By introducing the same error on the measurement of the previous case is introduced.

Error (4.8) [%]	Error (4.7) [%]	Computational time [s]
8.35 ± 0.0450	5.12 ± 0.0089	6.71 ± 0.16

Table 4.7. Variation of the error considering an error, SVT, spiral

Considering now a $\lambda/10$ sampling, the variation of the error computed as (4.8) with respect to the percentage of measured points is listed in Table 4.8 :

In Figure 4.7 is shown the case where the 20% of points have been measured. For the spiral path $A=0.13$ while $\omega=1.35$.

Percentage of measured points [%]	Error with frobenius norm, (4.7),[%]
5	82.4
10	52.0
15	31.6
20	14.5
25	8.14

Table 4.8. Variation of the error wrt percentage of measured points, svt, spiral path

4.4 COMPARISON BETWEEN SVT AND CVX

In this section will be shown the results of the technique used in Chapter 3, that considers the use of first an interpolation through the splines for the points not measured and then a nuclear norm minimization using the CVX software, and of the method explained in this chapter, that considers the use of the SVT algorithm for the nuclear norm minimization without using a previous splines interpolation. In order to compare the two technique, a $\lambda/5$ sampling has been considered, since performing a $\lambda/10$ sampling, and in practice have an amount of 25600 to manage, would have requested a huge effort in term of computational time for using the CVX software. The scattering object has been considered a 4x4 array of helix antennae, as seen in Figure 4.2. All the parameters of the scattering object are the one declared in the section 2.3.

To evaluate the differences the radial and the spiral trajectories are considered; moreover, it has been simulated even the case when the points are not selected according to a determinist trajectory but randomly. In this last case, an average between 10 simulations are done.

Since one of the aims is to minimize the time flight of the drone, the idea is

to measure less samples than required by the Nyquist criterion according to the electric size of the antenna. The Nyquist sampling theorem states that a continuous signal, $y(t)$ with a frequency f_M , can be reconstructed from its sampled signal $y(n\Delta t)$ if signal is sampled with a frequency $f_S \geq 2f_M$. In our case, to perform an undersampling less than the 16% of total amount of points shall be measured.

The reconstruction error is computed using the formula (4.8), using the Frobenius norm.

Percentage of measured points [%]	Error CVX [%]	Error SVT [%]
5	78.1	80.0
10	71.2	70.6
15	59.3	51.2
20	45.8	36.2

Table 4.9. CVX and SVT error, spiral path

Percentage of measured points [%]	Error CVX [%]	Error SVT [%]
5	42.2	32.5
10	32.9	25.2
15	15.6	11.6
20	14.6	8.42

Table 4.10. CVX and SVT error, radial path

As it is possible to see from the tables, the SVT algorithm has better results than the CVX software, except for the case of random selection points. For both methods, the results are smaller when a radial trajectory is used.

Taking into account even the computational time for the simulation, the CVX

Percentage of measured points [%]	Error CVX [%]	Error SVT [%]
5	68.1	85.8
10	43.6	56.7
15	28.9	41.8
20	18.4	25.4

Table 4.11. CVX and SVT error, random selection

software needs more or less of 10 minutes while the SVT algorithm less than 30s, in the case of a $\lambda/5$ sampling; the difference gets bigger when it is considered a $\lambda/10$ sampling: the SVT runs in less than 1 minute while the CVX software needs around 2 hours.

Anyway, even if it is possible to treat with bigger matrices by using the SVT algorithm, the error on the reconstruction of the field is still not negligible when less samples than required by the Nyquist's criterium are measured. There is still the need to measured around the 30% of points to have an error less than the 5% in the case of a radial path, while around 40% of points if a spiral trajectory is considered.

In the following chapter will be introduced a new technique with who it will be possible to overcome this problem. Unlike the two methods analysed so far, it doesn't rely on matrix completion algorithm.

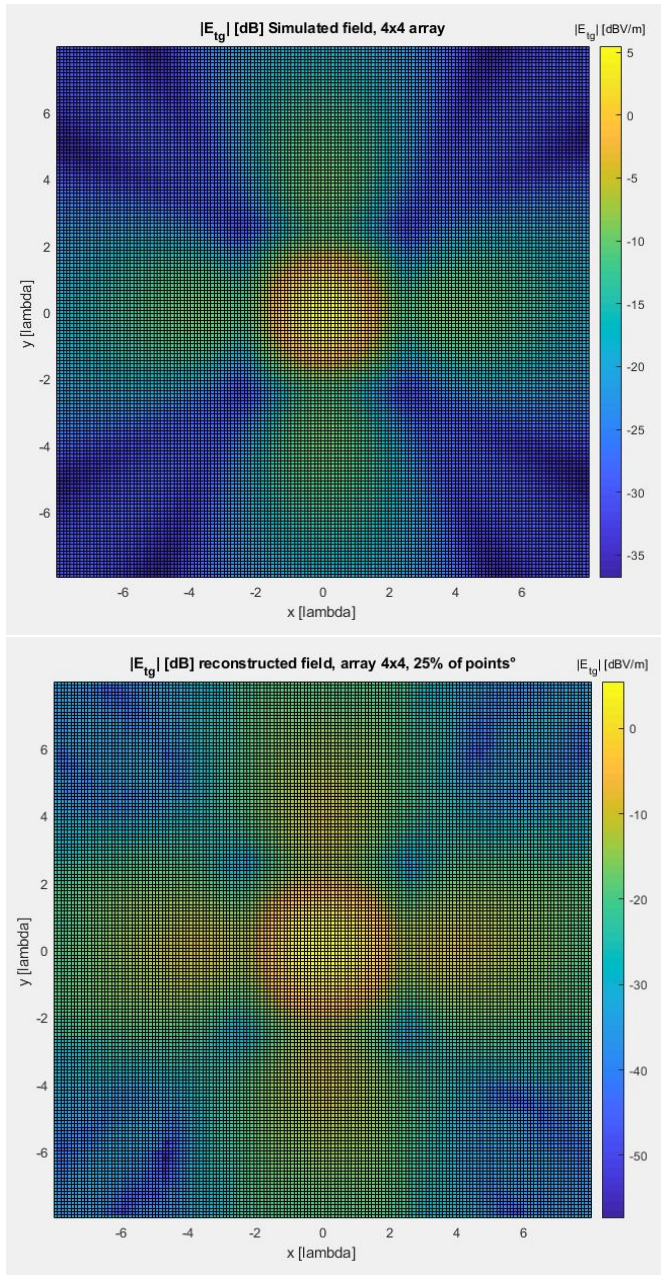


Figure 4.4. Original and reconstructed field, svt, radial path, 20% of points, $\lambda/10$ sampling

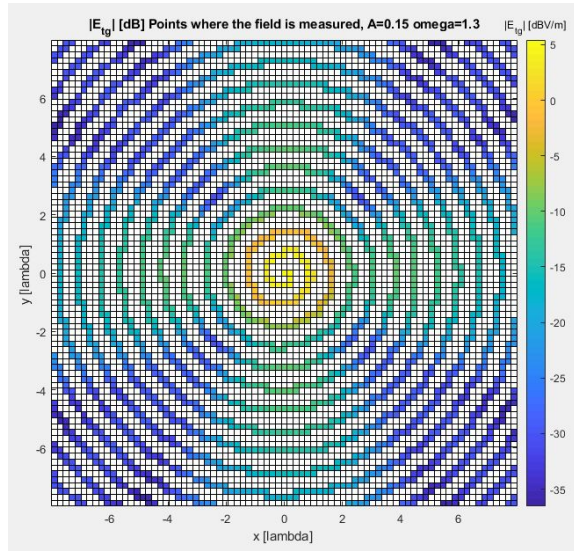


Figure 4.5. Measured points setting $A=0.15$ and $\omega=1.3$

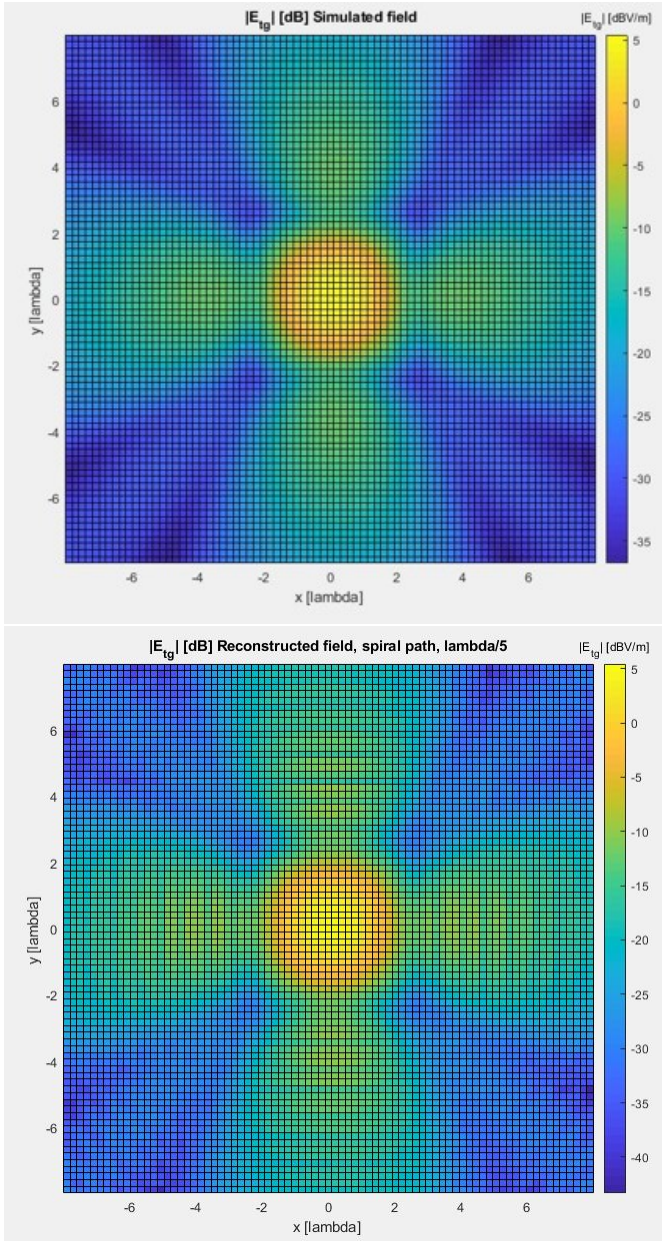


Figure 4.6. Reconstructed field with the spiral path, $\lambda/5$

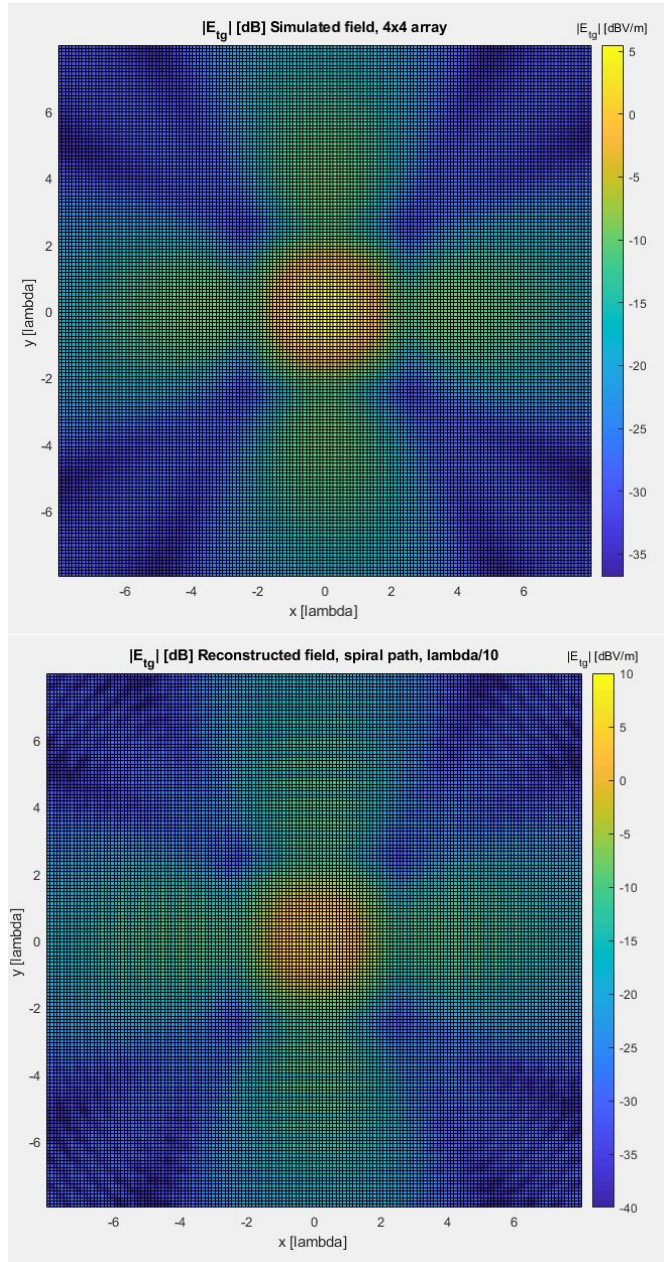


Figure 4.7. Reconstructed field with the spiral path, $\lambda/10$, 20% of points

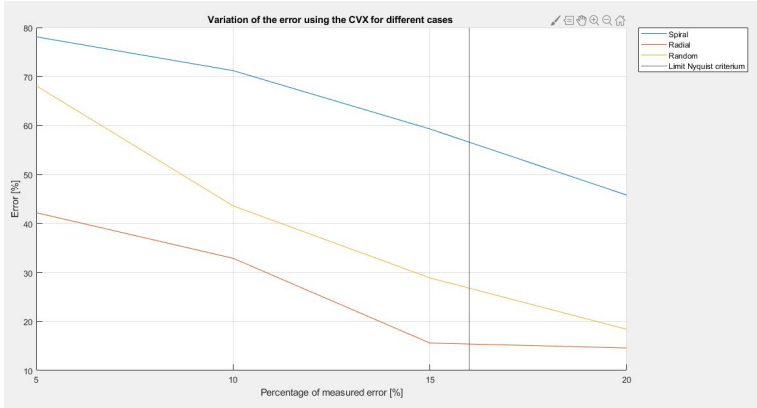


Figure 4.8. Graphics that shows the behaviour of the results obtained using the CVX software

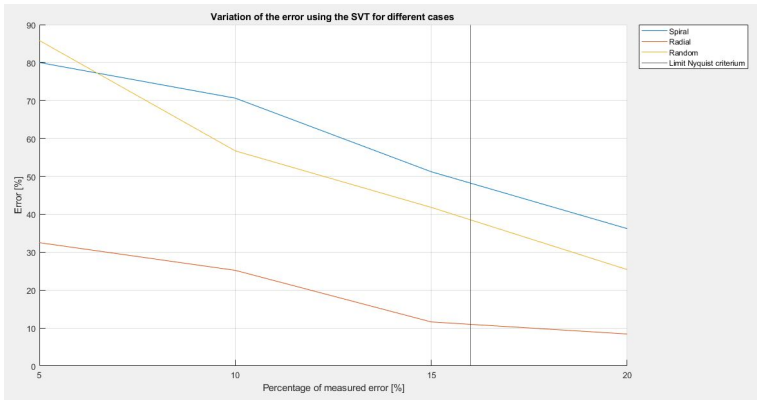


Figure 4.9. Graphics that shows the behaviour of the results obtained using the SVT algorithm

Chapter 5

REDUCED ORDER MODEL

In this chapter a new technique for the reconstruction of the electromagnetic field is introduced. So far, two methods have been exploited that allow obtaining the near field scattered by the radiating source, but it has not been mentioned how to compute the far field once the near field is known. With the procedure described in this chapter, both the near field and the far field radiated by the antenna can be computed, starting from the same input.

The procedure relies on a reduced order model (ROM) for antenna characterization.

So far, only the situation when the samples are taken on a regular matrix surface has been analysed; here, in addition to this, also the situation where the samples are taken on an irregular surface, coincident with the trajectory of the drone will be studied.

The characteristic of the scattering object have been introduced in Section 2.3. Here, will be analysed a single helix antenna and an array of 2x2,3x3 and 4x4 helix antennae.

Before to introduce the new technique, a brief introduction to the equivalence theorem, also known as the Love's theorem, is necessary.

5.1 LOVE'S THEOREM

Let's suppose to have a generic electric source \mathbf{J} , and/or a generic magnetic source \mathbf{J}_m , that induce in the space an electromagnetic field that can be described by the couple (\mathbf{E}, \mathbf{H}) , obeying the Maxwell's laws introduced in the formula (2.3); moreover, let's consider a generic closed surface S that encloses the sources, with the assumption that the surface S is compact and it is possible to define a normal component $\hat{\mathbf{n}}$ for all the boundary points.

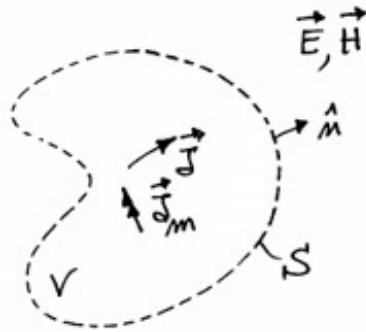


Figure 5.1. Starting condition of the Love's theorem

Given this hypothesis, it is possible to substitute \mathbf{J} and \mathbf{J}_m with new equivalent sources, \mathbf{J}_s and \mathbf{J}_{ms} , that belong to the surface S. The linkage of the new sources with the previous couple of the field is given by:

$$\begin{cases} \mathbf{J}_s = \hat{\mathbf{n}} \times \mathbf{H}_s \\ \mathbf{J}_{ms} = -\hat{\mathbf{n}} \times \mathbf{E}_s \end{cases} \quad (5.1)$$

In the formula (5.1) \mathbf{H}_s and \mathbf{E}_s are respectively the magnetic and electric field scattered by the sources \mathbf{J} and \mathbf{J}_s , computed on the surface S. The new sources, \mathbf{J}_s and \mathbf{J}_{ms} , generates a new couple of the field, $(\mathbf{E}', \mathbf{H}')$. This new couple is equal to the previous one (\mathbf{E}, \mathbf{H}) outside the surface S, while inside it the field is equal to zero [11]. The new situation is summarized in the figure 5.2.

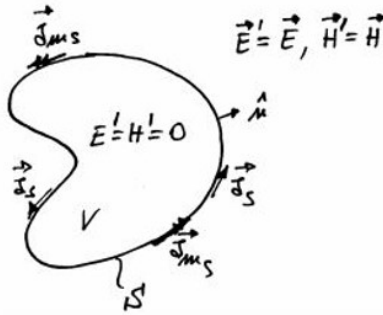


Figure 5.2. Final condition of the Love's theorem

In the following, the surface S that encloses the antenna under test will be a parallelepiped, with dimension of $(2\lambda, 2\lambda, 2.5\lambda)$ in the case of a 3-3 and 4-4 array, while in the case of a single helix and in the case of a 2-2 array the dimensions are

$(\lambda, \lambda, 2.5\lambda)$.

5.2 REDUCED ORDER MODEL METHOD

A reduced order model (ROM) is a simplification of a more complex model. It is useful to introduce it because it reduces the computational complexity of the complex original model. It is possible to obtain a simplified version from a complex model by reducing the state space dimension or the degrees of freedom. [21]. An important assumption is that the input-output relation of the original model is still preserved when the ROM is built. Here, the properties of the ROM relies on the knowledge of a small amount of data to be measured, on the outer dimension of the antenna and on geometry of the measurement surface scan; no a priori information on the characteristic of the radiated source are necessary.

The ROM is built on the base of the article [22]. Let's suppose to have a generic antenna that radiates in the space, and assume to enclose the antenna with an arbitrary closed surface S . The input is given by the equivalent electric, or magnetic, currents \mathbf{J}_s and \mathbf{J}_{ms} on the surface S introduced in (5.1); the output is the radiated far field, or the near field, of the antenna on a surface S' . The two surfaces, for hypothesis, are distinct.

The electric field computed on the surface S' at a generic position \mathbf{r}' depends only on the equivalent sources on the surface S [22]. The relation is given by :

$$\mathbf{E}(\mathbf{r}') = \int_S \bar{\mathbf{G}}_{EJ}(\mathbf{r}'|\mathbf{r}) \cdot \mathbf{J}_{EQ}(\mathbf{r}) dS \quad (5.2)$$

In the formula (5.2), $\bar{\mathbf{G}}_{EJ}$ is the electric field free space dyadic Green function for

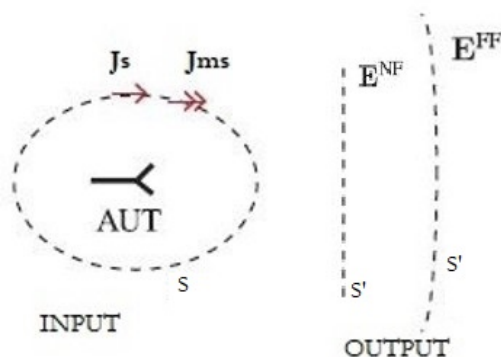


Figure 5.3. Scheme of input-output for the ROM

electric sources. By discretizing the two surfaces S and S' it is possible to write the formula (5.2) in a matrix-vector form, as follow:

$$\mathbf{e} = \mathbf{G} \mathbf{j}_{eq} \quad (5.3)$$

The vector \mathbf{e} represents the discretized electric field tangential to the surface S' , the vector \mathbf{j}_{eq} represent the discretized equivalent electric and magnetic currents on the surface S , while \mathbf{G} is the so called radiation matrix, that maps any current distribution on S to the radiated field S' .

The problems now becomes to compute the equivalent currents \mathbf{j}_{eq} on the surface S . The first step is to measure some samples of the electric field \mathbf{e} in a generic position (\mathbf{r}') from the antenna under test. In our specific case, these samples are taken by means of a drone in the near field region, according to different trajectories that will be introduced later. Then, the radiation matrix \mathbf{G} is built. At this stage, from the relation (5.3) it is possible to compute \mathbf{j}_{eq} . Since our interest is to minimize the quantity $\|\mathbf{G} \mathbf{j}_{eq} - \mathbf{e}\|$, the equivalent currents are computed with the Matlab

command `lsqr`, that attempts to solve the least squares solution \mathbf{j}_{eq} that minimizes the previous quantity. Consequently, to evaluate the performance of the procedure, the error is computed as:

$$\frac{\|\mathbf{G}\mathbf{j}_{eq} - \mathbf{e}\|}{\|\mathbf{e}\|} \quad (5.4)$$

At this stage, once the equivalent currents on the surface S are obtained, for the input-output relation of the ROM it is possible to compute both the far field and the near field radiated by the antenna under test.

The trajectories with which the near field is computed are the spiral and radial introduced in the previous chapter 3. Moreover, to these two trajectories, other two are added; they come from by joining together some points given as output of a discrete empirical interpolation method (DEIM).

5.3 DISCRETE EMPIRICAL INTERPOLATION

The radiating operator \mathbf{G} is compact because the surfaces S and S' are distinct for hypothesis. For definition, a compact operator T is a linear operator from the Banach space such that: $T : X \rightarrow Y$; an important property is that T is a bounded operator, so it is continuous [23]. Since \mathbf{G} is bounded it is possible to compute its singular value decomposition (SVD) and it can be written in a factorized form: [24] :

$$\mathbf{G} \approx \mathbf{U}\mathbf{\Sigma}\mathbf{V}^* \quad (5.5)$$

With this procedure only the r largest singular values σ_r are kept. The matrix \mathbf{U} has a size of $M \cdot R$, where M is the length of the vector \mathbf{e} . The value M is related to the number of measured points. The r singular values σ_r quantify the amount of power that is coupled from one characteristic mode of S to S' [22]. At this stage, the DEIM algorithm is applied to the matrix \mathbf{U} in order to identify the dominant equivalent electric currents. The output of the DEIM is a sorted list of points, from the most to the least significant ones, that has to be measured in order to properly characterize the antenna under test.

An example of how the DEIM works is given in Figure 5.4. On the left there is the simulated electromagnetic field scattered by a 4×4 array of helix antennae, with a $\lambda/10$ sampling; by building the radiation matrix \mathbf{G} that goes from S to S' for this specific antenna under test, it is possible to apply the DEIM algorithm. On the right side of the Figure 5.4 is shown the most significant points selected by the DEIM to have a fast characterization of the antenna under test. Once that these points are obtained, they have to be measured by the drone, so the problem now becomes finding a trajectory that passes through or in the nearby of the points.

Since the aim is to minimize as much as possible the flight time of the drone, consequently, the covered path, it is necessary to find a minimum path between all the points given by the DEIM. For this purpose, the kinematic and dynamic constraints of the drone haven't been taken into account, but only a fast solution was found, based on the minimization of the Euclidean distance between all the points. A so formulated issue can be seen as an instance of the Travelling Salesman problem (TSP); an example of how the TSP is solved can be found in [25].

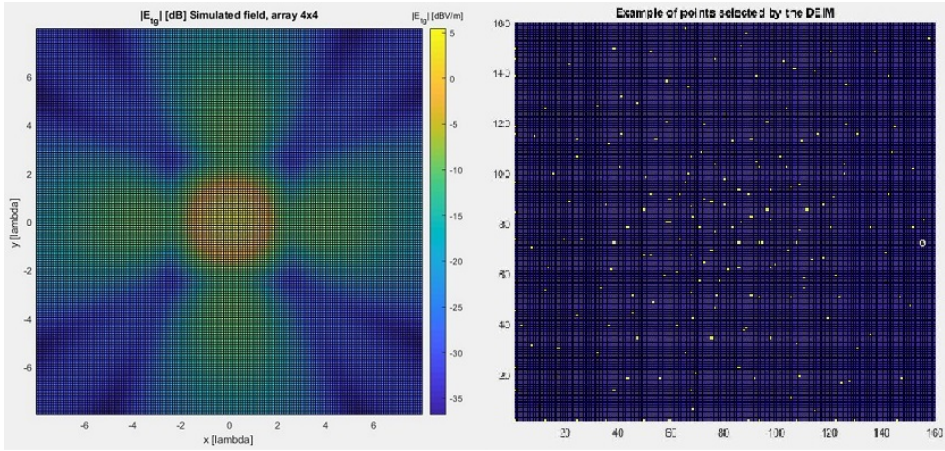


Figure 5.4. Example of the points selected by the DEIM

An easy way to find the exact solution for the TSP would be to try all the permutations of the points and find what is the minimum distance covered. A so formulated algorithm has a computational complexity of $O(N!)$, where N is total number of the points. In the thesis, the maximum value of N is 360, in the practice becomes impossible to find a correct solution of the TSP problem. For this reason, a heuristic algorithm is considered. In particular, the Nearest Neighbour (NN) algorithm is used; its computational complexity in the worst case is $O(N)$ [26]. In this thesis, the Matlab NN algorithm used has been written by Aleksandar Jevtic in the 2009, and it can be found in the Mathworks File Exchange; unlike the original algorithm, where the points are selected randomly from a list of cities, here are exactly the points given by the DEIM. The algorithm works following these steps:

- i. Select a current point;
- ii. Find out the shortest distance between the current point and the remaining not-visited points;

- iii. Set a new point as the current one;
- iv. Mark the previous point as visited;
- v. If all the points have been already visited, terminate the algorithm, else go to step ii.

In this thesis, two distinct situations has been analysed: the former takes into account all the points of the DEIM; the latter selects only the first $2/3$ of points in order to have an easier trajectory for the drone to be followed.

The algorithm returns the length of the path and the list of the coordinates of the points of the matrix, ordered from the first to the last point to visit.

In the case of the near field, or the far field, analysed starting from an irregular measurement surface, two functions are considered for approximating a reliable path for the drone through the points: a cubic spline trajectory and a B-spline trajectory. Instead, in the case of a regular matrix surface, the points are simply connected by horizontal, or vertical, or diagonal movements across the squares of the matrix.

5.3.1 CUBIC SPLINE AND B-SPLINE TRAJECTORY

The definition of the spline has been introduced in Section 3.1. An important characteristic of a spline interpolation is that the interval of observation is subdivided in smaller intervals, and for each one of these is provided a mathematical function of a certain degree; moreover, the splines provide a certain smoothness, depending on the degree of the spline interpolation, at places where the polynomial pieces connect [27]. Since a spline interpolation is smoother than interpolating with other

methods, such as a polynomial interpolation, it is preferred because the drone can follow easier the trajectory.

The cubic spline provides a third degree polynomial for each sub-interval of the set of interpolating data; for each sub-interval, the cubic spline can be described as a time-dependent function of the form:

$$\mathbf{q}(t) = a_0 + a_1t + a_2t^2 + a_3t^3 \quad (5.6)$$

With this choice, in each sub-interval the function admits a second derivative, that corresponds to the acceleration profile, and the value of the second derivative computed at the edges of each interval is equal to zero.

The B-spline, called also basis spline, is a Bézier curve with a minimal support with respect to a given degree, smoothness and domain partition [27]. The main difference with respect to the other spline method interpolation is that the evaluation of the B-spline is based on a recursive procedure instead of a closed form expression [28].

Assuming a B-spline of a degree p and a number N of waypoints, the parametric curve $\mathbf{s}(t)$ is described by the following equation [29] :

$$\mathbf{s}(t) = \sum_{i=0}^N \mathbf{p}_i B_i^p(t) \quad (5.7)$$

The vectorial coefficients \mathbf{p}_i^p are called control points and they determine the shape of the curve and they are computed imposing interpolation conditions on the set of data points. The quantities B_i^p are the i -th B-spline basis function of degree p and they are definite in a recursive way. The formula for the B-spline basis function can be found in [29].

The cubic spline trajectory has been computed by means the Matlab command *spline*, while for the B-spline trajectory the Matlab command *bsplinepolytraj*. For both cases, the function returns at any given time the position on the (x,y); the time interval has chosen as $t = [0 : 0.01 : 200]$. The trajectories are uniformly sampled between the start and end times of the interval. The total length (dist) of the path has been computed as:

$$dist = \sum_{i=0}^{J-1} \sqrt{(p_{xi} - p_{x(i+1)})^2 + (p_{yi} - p_{y(i+1)})^2} \quad J = 2 \cdot 10^4 \quad (5.8)$$

The formula is the summation of the Euclidean distance between the i-th and (i+1)-th points.

The cubic spline trajectory passes exactly through the waypoints given by the DEIM while the B-spline trajectory falls inside the polygon defined by the control points \mathbf{p}_i^p . In Figure 5.5 is shown an example of the different of the two trajectories, using the same waypoints and the same path.

5.4 RECONSTRUCTED NEAR FIELD

As mentioned in the section above, now will be analysed not only the case where the points are taken on a regular matrix surface, that can be represented by a square matrix, but even the case where the points are taken according to an irregular surface, coincident with the path of the drone.

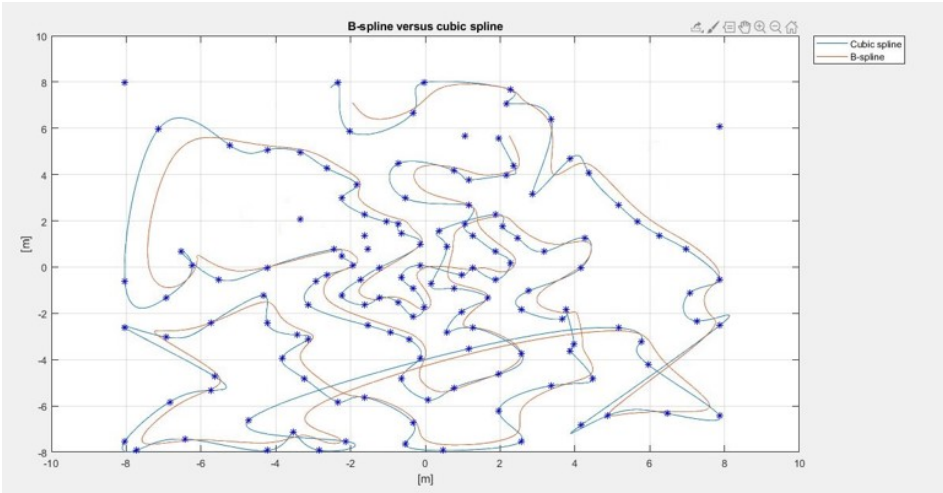


Figure 5.5. Difference between cubic spline and B-spline

5.4.1 REGULAR SURFACE

The matrix that represents the surface goes from -8λ to $+8\lambda$, with the value of $\lambda = 1.45m$ and it has been performed a $\lambda/10$ sampling on both x and y axis. As a result, the electromagnetic field is represented by a 160×160 matrix. The procedure is briefly explained in the following.

As done in the previous chapters, a certain number of samples are taken from the matrix by means of a radial and spiral trajectory; in this subsection, also a trajectory that connects all the points, and the $2/3$ of the points, given as the output of the DEIM is considered; moreover, it has been simulated also the case when only the points, and the $2/3$ of points, are considered as the basis for the reconstruction of the field.

The equivalent currents \mathbf{j}_{eq} are computed as $\mathbf{j}_{eq} = lsqr(\mathbf{G}_{\tilde{t}ilde}, \mathbf{e}_{indices})$, where the matrix $\mathbf{G}_{\tilde{t}ilde}$ is obtained by considering only the rows and all the columns of

the radiation matrix, \mathbf{G} , in correspondence of the x,y,z coordinates of the points below the trajectory of the drone; in a few words, $\mathbf{G}_{\tilde{t}} = \mathbf{G}(\text{indices}, :)$ where indices indicates the x,y,z coordinates of the measured points by means of the drone or by considering the points given by the DEIM; the size of $\mathbf{G}_{\tilde{t}}$ is M·N, where M is three times the number of measured points and N is the number of the basis vector; the size of the matrix G follows the electrical size of the surface S and S'. The matrix $\mathbf{e}_{\text{indices}}$ contains all the value of the simulated field in the points that are measured; it is a column vector of a dimension of 3 times the number of measured points. As a result, \mathbf{j}_{eq} has a size of N·1. It is important to underline that the radiation matrix, \mathbf{G} , is always the same for each scattering object, i.e. it doesn't not depend on the considered trajectory.

The error is computed with the formula (5.4). The results are shown in the table 5.1 and in the figure 5.6. Since it has been considered a 160·160 matrix, the total amount of the points that represent the near field are 25600. It is important to underline that the DEIM selects 330 points to measure, that correspond an amount of 1.3% of the total points. By joining together all the points selected by the DEIM, the 35% of the points are measured, while by joining only 2/3 of the points given by the DEIM the amount of the measured points decreases to the 30%.

The penultimate row of the table refers to the case when all the points of the near field matrix are used to compute the equivalent currents \mathbf{J}_s . The last row refers to the case when it is measured a sample each $\lambda/2$ on both x and y axis, example in figure 5.7; in this case an amount of 0.04% points are measured.

The comparison between the different configurations of the arrays has been done

Trajectory	Er single [%]	Er 2x2 [%]	Er 3x3 [%]	Er 4x4 [%]
Spiral 10% points	0.87	0.79	2.17	8.23
Spiral 15% points	0.17	0.14	0.58	3.84
Radial 10% points	0.18	0.28	1.03	7.50
Radial 15% points	0.11	0.14	0.44	3.37
All points of DEIM	0.11	0.15	0.46	3.54
2/3 points of DEIM	0.12	0.16	0.48	3.71
Connecting all points	0.10	0.11	0.45	3.25
Connecting 2/3 points	0.11	0.10	0.46	3.37
All NF points	0.099	0.010	0.41	3.13
Uniform sampling $\lambda/2$	95	100	102	103

Table 5.1. Error computed as (5.4) for different cases

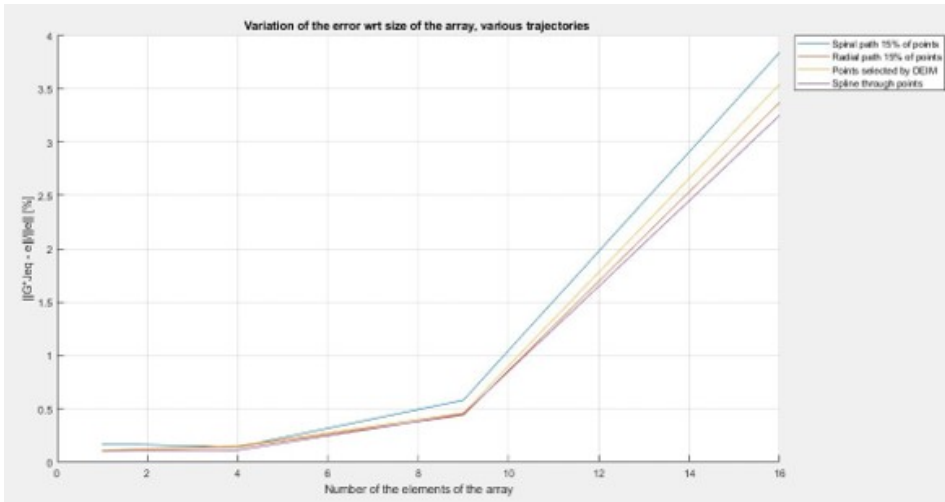


Figure 5.6. Behaviour of the error computed as (5.1) for different cases

by considering the above-mentioned dimension of the surface S and, by considering the same the same trajectory for all the cases regarding the spiral and radial; when it is considered the case when the points are connected joining together the output of the DEIM the trajectory changes by considering different arrays, but anyway they have the same percentage of measured points. Moreover, it is needed

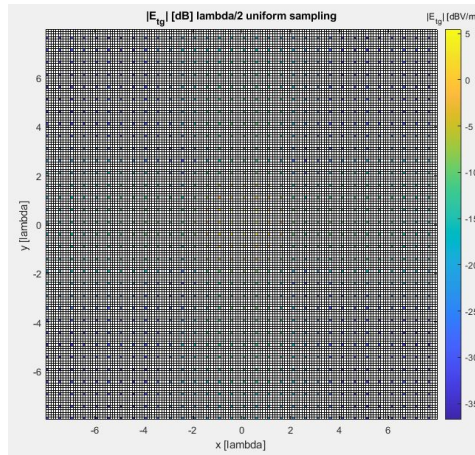


Figure 5.7. Example of uniform $\lambda/2$ sampling

to underline the fact that, in the case of a radial and spiral path, it is possible to properly reconstruct the near field pattern even using less samples than required by the Nyquist's criterium (less than the 16% of measured points), since the obtained error can be considered small. This is an improvement with the respect the case when the CVX software (chapter 3) or the SVT algorithm (chapter 4) is used. In the following, an example of how the near field is reconstructed is shown; in particular, it is shown the case of the array 4×4 , reconstructed by a spiral and radial path, measuring only the 15% of points, all the points of the DEIM and when all the points of the DEIM are joint together.

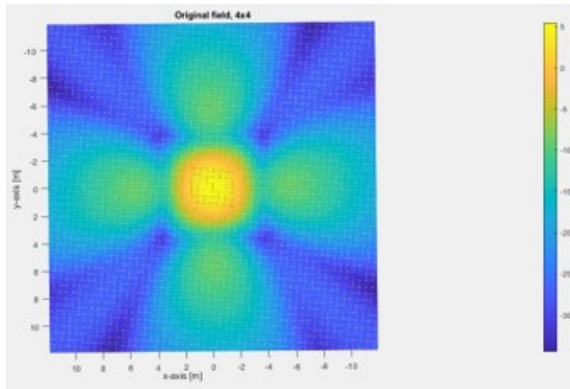


Figure 5.8. Original field, array 4x4, ROM

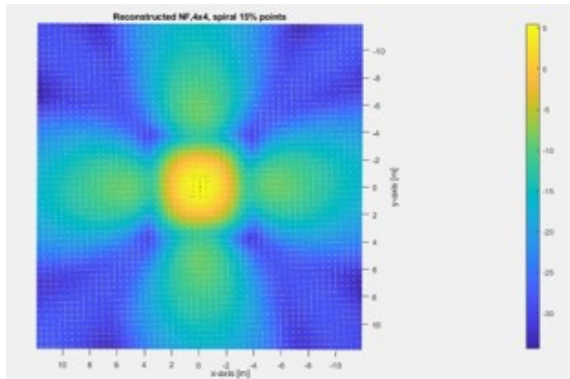


Figure 5.9. Reconstructed NF, spiral path 15% of points, 4x4, ROM

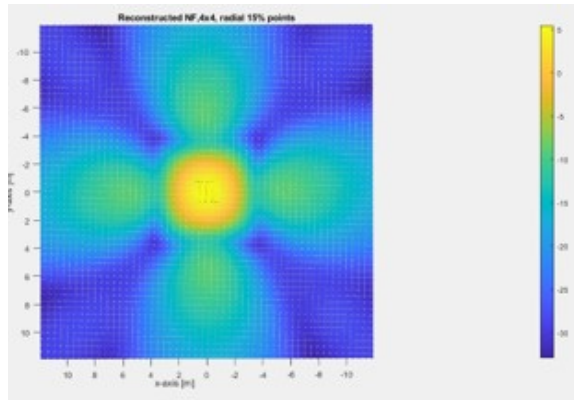


Figure 5.10. Reconstructed NF, radial path 15% of points, 4x4, ROM

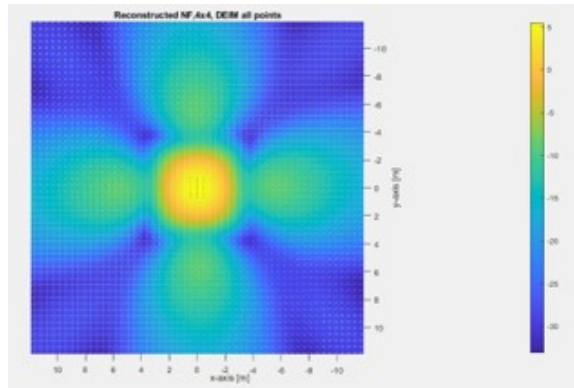


Figure 5.11. Reconstructed NF, all points of the DEIM, 4x4, ROM

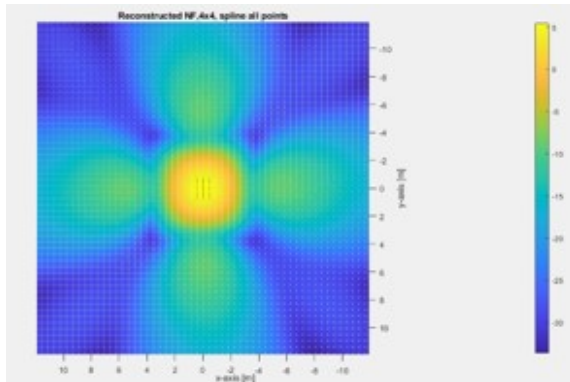


Figure 5.12. Reconstructed NF, joining all points of the DEIM, 4x4, ROM

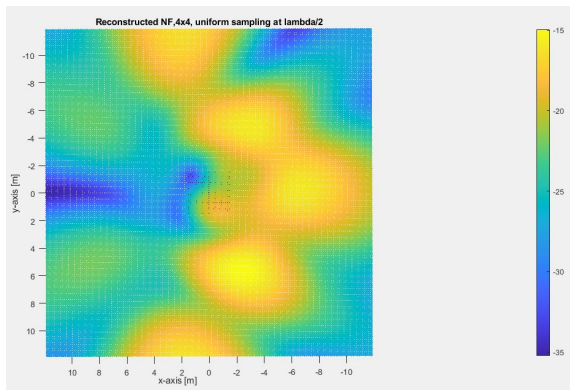


Figure 5.13. Reconstructed NF, uniform sampling $\lambda/2$, 4x4 ROM

5.4.2 IRREGULAR SURFACE

In this subsection it is shown the case when the surface is not a regular matrix surface, but it is coincident with the trajectory of the drone. The difference between the regular and irregular surface can be seen in the figure 5.14. On the left there is the regular surface, where the measured points are selected between the points

of the matrix; while for the irregular surface, the near field is computed for all the (x,y,z) coordinates that belong to the trajectory of the drone.

Here, the equivalent currents \mathbf{j}_{eq} are computed as $\mathbf{j}_{eq} = lsqr(\mathbf{G}, \mathbf{e})$. Unlike the

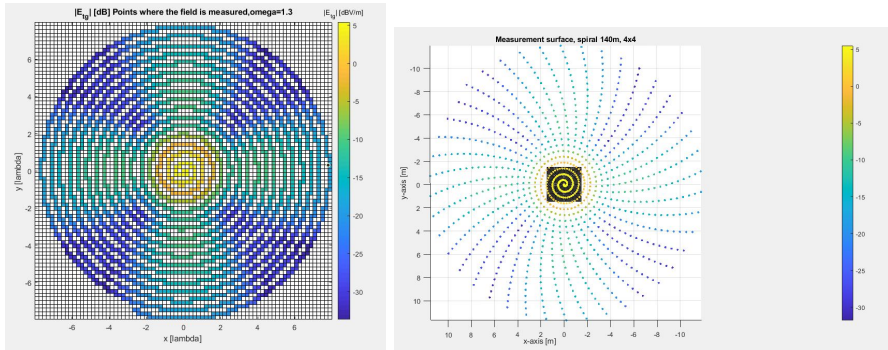


Figure 5.14. Difference between a regular and irregular surface

previous case, the radiation matrix, \mathbf{G} is not equal for all the cases for each scattering object, but it depends on the particular trajectory, or more in general on the measured field \mathbf{e} . The size of \mathbf{G} is $m \cdot n$, where m is 3 times the number of the measured points and n is the number of the basis vectors of the scattering object; the vector \mathbf{e} is column vector of size m ; as a consequences, the vector \mathbf{j}_{eq} is a column vector of size n . In order to evaluate the algorithm, it is computed the error as in the case (5.4).

An important issue to solve is the total length of the trajectory. How long the trajectory should be to correct evaluate the performance of the procedure?

To answer this question it has been taken into account the cubic spline and the B-spline trajectories. By considering the case of a single helix antenna, once the radiation matrix has been obtained in the subsection 5.4.1, and once the SVD decomposition has been performed as (5.5), the DEIM algorithm is applied to the

matrix \mathbf{U} . At this stage, the TSP algorithm is applied only to the first 2/3 of points given as output of the DEIM and as a result it is given a list of points to travel for minimizing the length. Then, a cubic spline and a B-spline trajectory has found in order to connect all the points.

With this procedure, the cubic spline trajectory has a length of 173m while the B-spline is 140m. In order to properly compare the trajectories, it has been considered also a spiral and a radial trajectory with a length of 173m and 140m.

Even if these lengths have been computed by considering the radiation matrix of the single helix antenna, they are fixed even for the others array, in order to evaluate the error for all the scattering objects by keeping constant the length of the trajectory.

The results are shown in Table 5.2 and Table 5.3.

In Table 5.4 the results in the case of a uniform $\lambda/2$ are shown. The measured points are shown in Figure 5.15

Trajectory [140m]	Er single [%]	Er 2x2 [%]	Er 3x3 [%]	Er 4x4 [%]
Spiral	0.093	0.098	0.20	1.40
Radial	0.093	0.10	0.16	1.42
B-spline	0.11	0.096	0.16	1.15

Table 5.2. Error computed as (5.4) for different cases, lenght trajectory 140m

Trajectory [173m]	Er single [%]	Er 2x2 [%]	Er 3x3 [%]	Er 4x4 [%]
Spiral	0.095	0.098	0.29	1.40
Radial	0.090	0.097	0.31	1.77
Cubic spline	0.098	0.10	0.16	1.39

Table 5.3. Error computed as (5.4) for different cases, lenght trajectory 173m

To evaluate the performance between the irregular and regular surface, it is com-

Trajectory [173m]	Er single [%]	Er 2x2 [%]	Er 3x3 [%]	Er 4x4 [%]
Uniform $\lambda/2$	0.01	0.01	0.06	0.12

Table 5.4. Error computed as (5.4) in the case of a uniform $\lambda/2$ sampling

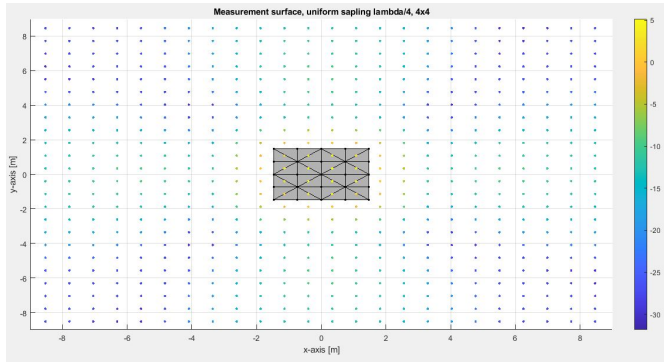


Figure 5.15. Irregular surface in the case of a uniform $\lambda/2$ sampling

puted the error in the case of spiral trajectory for a regular matrix with a length of 140m and 173, as in Figure 5.16. The results are compared with the case of the irregular surface and shown in Table 5.5 and in Figure 5.17. As it is possible to notice, the error is always smaller in the case of an irregular surface.

Trajectory	Er single [%]	Er 2x2 [%]	Er 3x3 [%]	Er 4x4 [%]
Spiral 140m	0.30	0.21	0.95	5.10
Spiral 173m	0.18	0.14	0.61	3.96

Table 5.5. Error computed as (5.4) spiral trajectory on regular surface

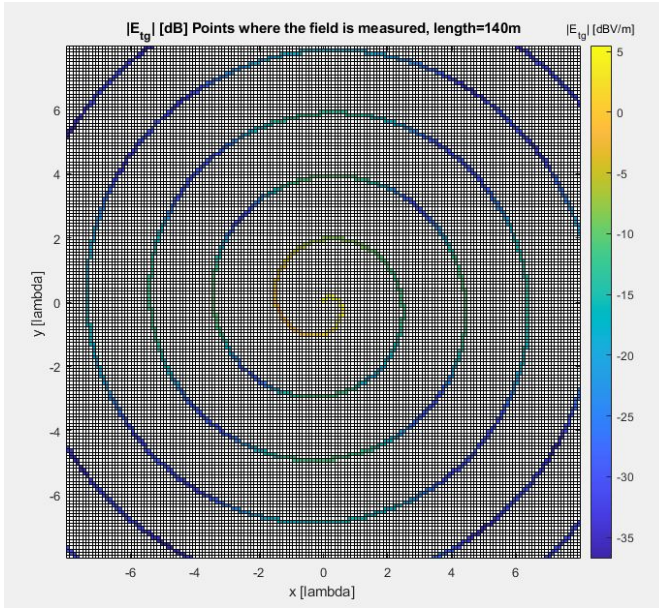


Figure 5.16. Spiral trajectory of 140m regular surface

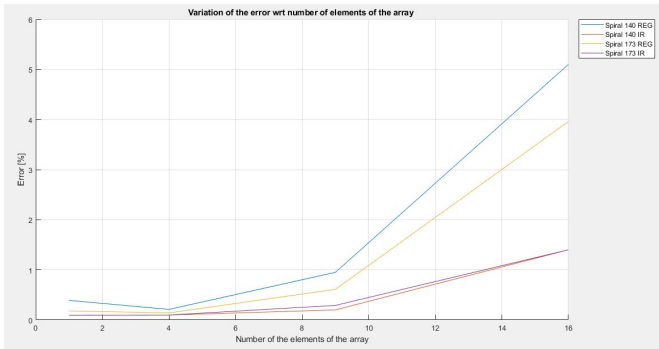


Figure 5.17. Error for irregular and regular surface, spiral trajectory

5.4 – RECONSTRUCTED NEAR FIELD

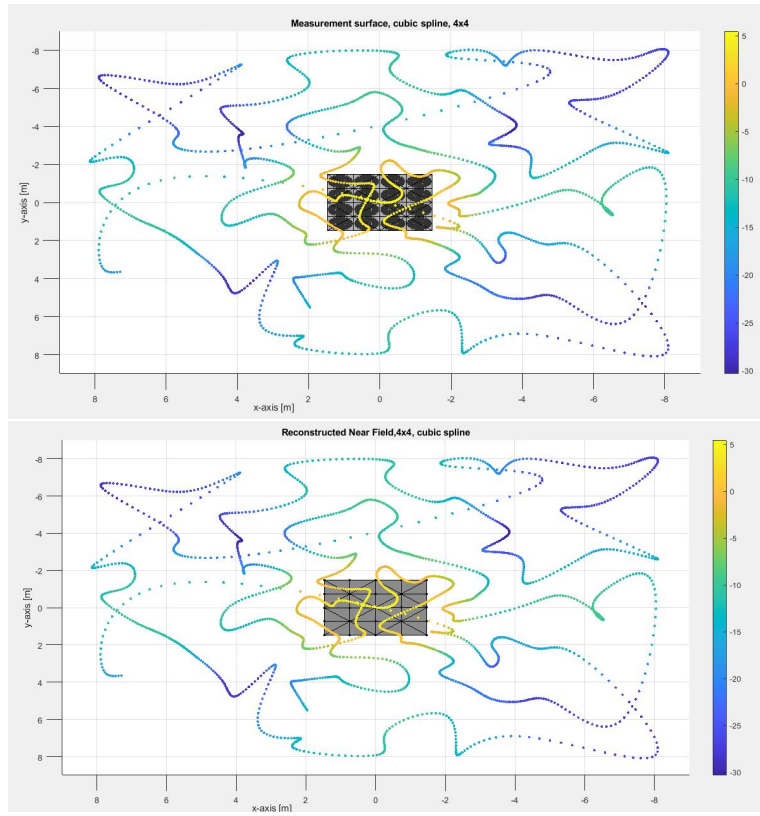


Figure 5.18. Original NF and reconstructed NF for cubic spline

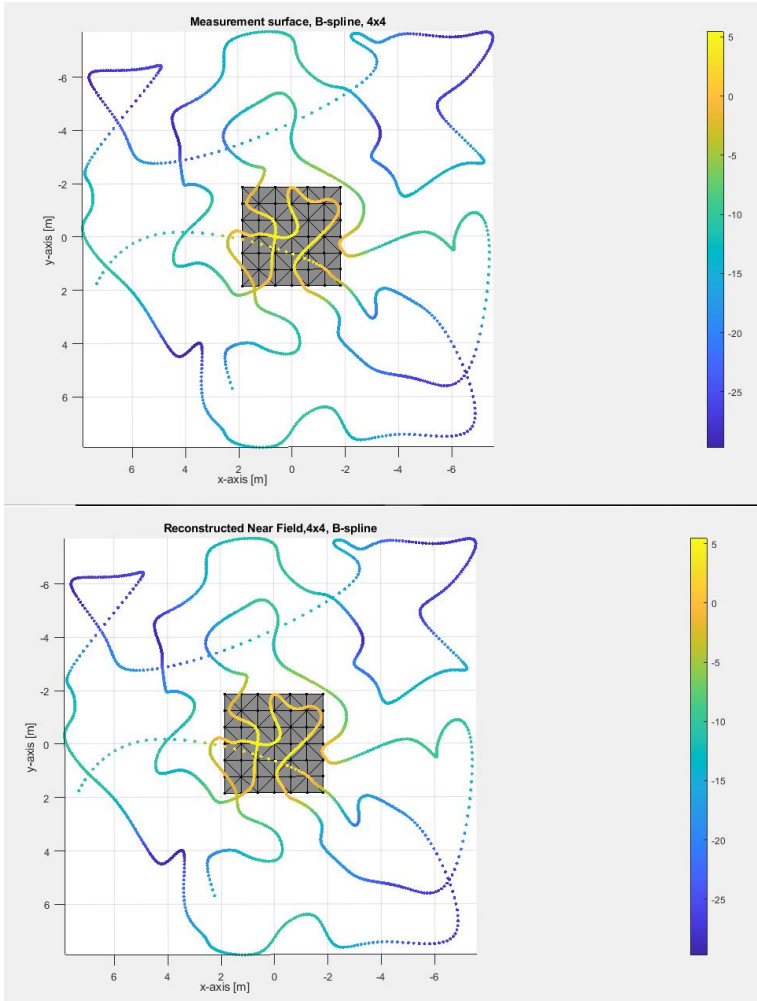


Figure 5.19. Original NF and reconstructed NF for B-spline

5.4 – RECONSTRUCTED NEAR FIELD

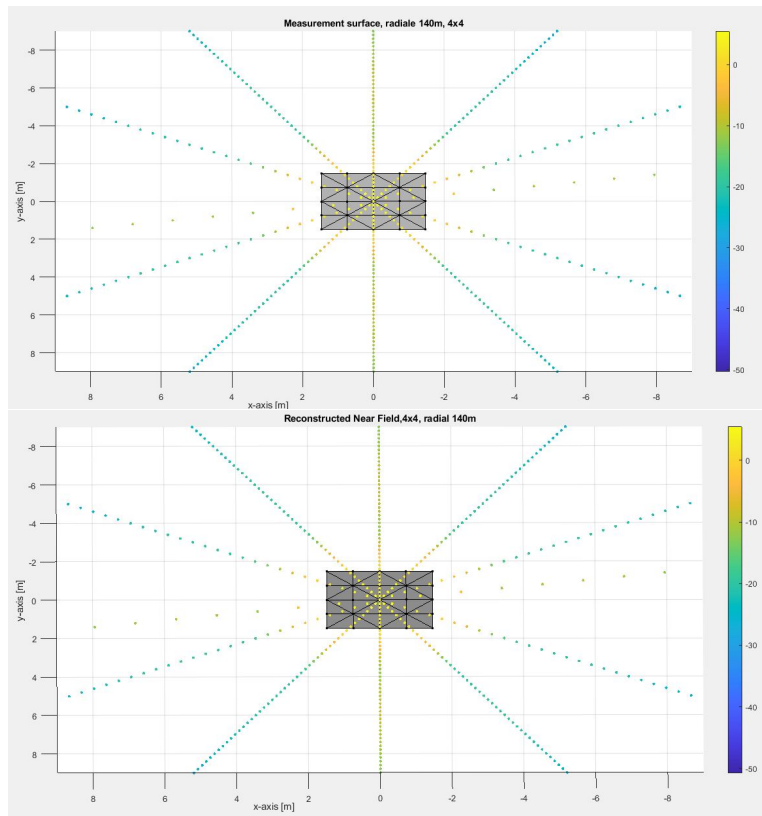


Figure 5.20. Original NF and reconstructed NF for radial trajectory 140m

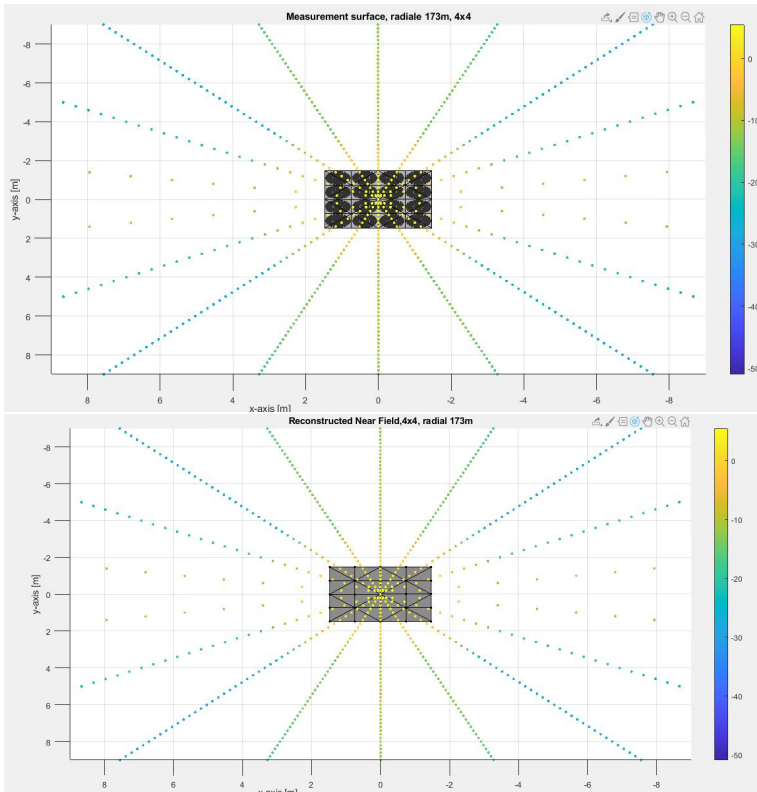


Figure 5.21. Original NF and reconstructed NF for radial trajectory 173m

It is possible to notice from the B-spline and cubic spline trajectory that the sampling is not uniform, but there are some areas where there is more space between a samples and its successor. This is due to the fact that the trajectories have been

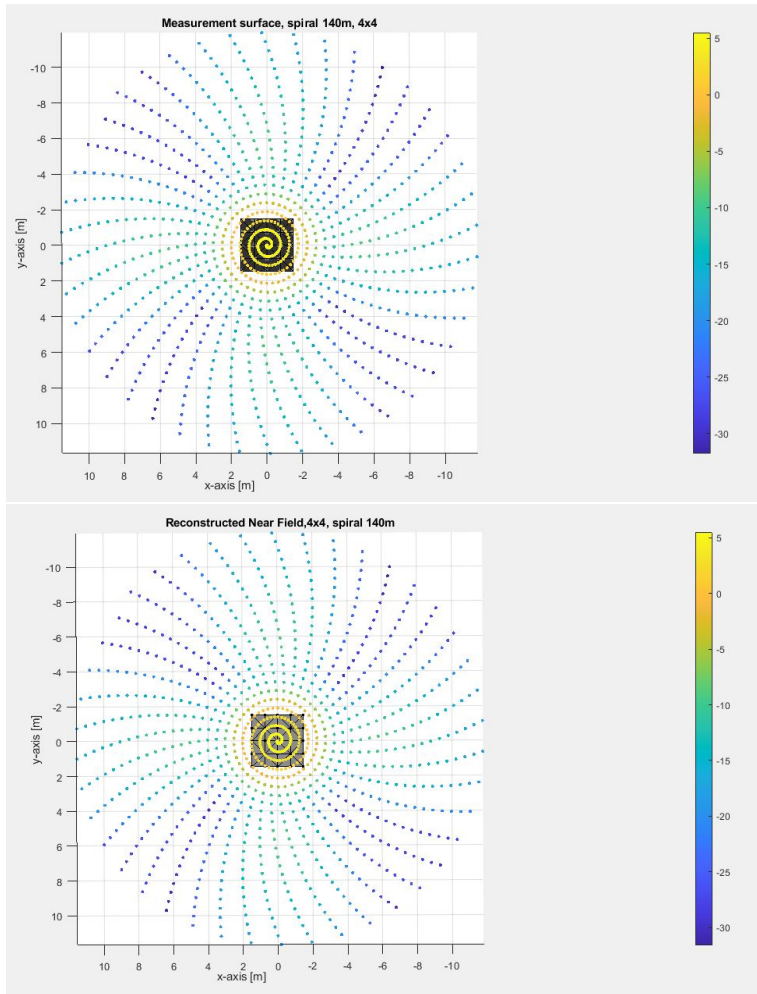


Figure 5.22. Original NF and reconstructed NF for spiral trajectory 140m

generated with a sampling time of 0.01s and that areas represents an acceleration of the drone. Whereas, for the spiral and radial trajectory, in order to make faster the simulation the chosen sampling time was to 0.1s. In the following is shown the error when the equivalent currents, \mathbf{j}_{eq} are computed starting from the points that

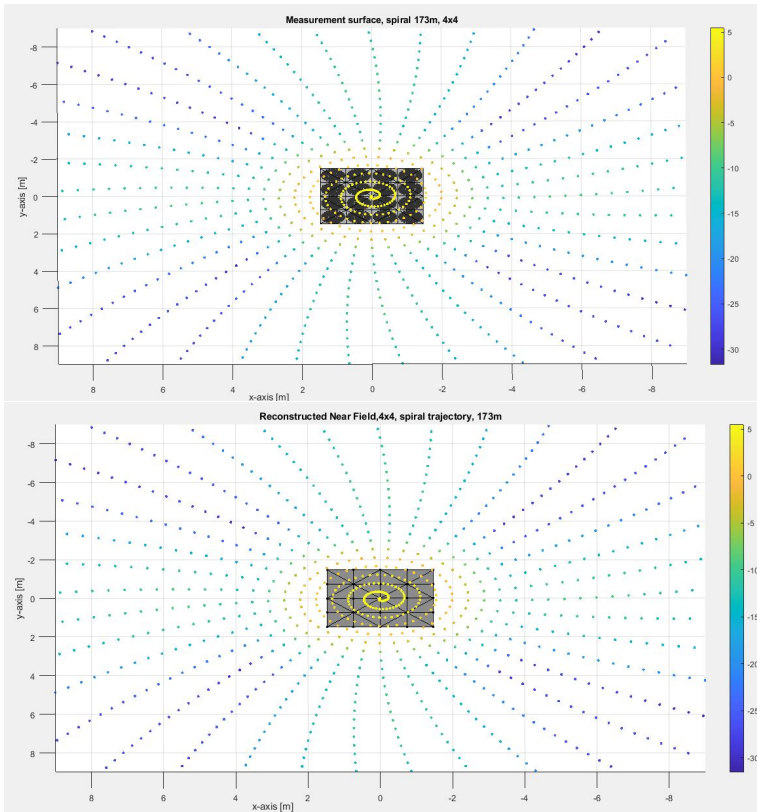


Figure 5.23. Original NF and reconstructed NF for spiral trajectory 173m

stay below the cubic spline and the B-spline trajectory generated by considering all the points of the DEIM, and not all the first 2/3 of points as in the previous case.

From the figures it is possible to see that with the use of the equivalent currents \mathbf{j}_{eq} it is possible to properly reconstruct the near field in the measured points.

Trajectory	Er single [%]	Er 2x2 [%]	Er 3x3 [%]	Er 4x4 [%]
Cubic spline	0.099	0.099	0.23	1.75
B-spline	0.095	0.088	0.22	1.67

Table 5.6. Error computed as (5.4) for cubic and B-spline considering all the points of the DEIM

5.5 RECONSTRUCTED FAR FIELD

In this section it will be shown the reconstructed far field radiated by the antenna, starting from the equivalent currents, \mathbf{j}_{eq} , computed as in the subsection 5.4.2. In this case, it is necessary to distinguish between the equivalent electric currents, $\mathbf{j}_{current}$, and the equivalent magnetic currents, $\mathbf{m}_{current}$. Supposing that \mathbf{j}_{eq} is a column vector of size $n \times 1$, it results that: $\mathbf{j}_{current} = \mathbf{j}_{eq}(1 : \frac{n}{2}, 1)$ and $\mathbf{m}_{current} = \mathbf{j}_{eq}(\frac{n}{2} + 1 : n, 1) * \eta_0$. The obtained far field is compared with the original simulated far field scattered by the considered array. Here are shown the results in the case of a 4x4 array for all the analysed trajectories.

In the following figures, the reference far field radiated by the antenna under test is compared with the reconstructed one. Two cases are shown: the case when the antenna is Right Hand Circular Polarized (RHCP) and when the antenna is Left Hand Circular Polarized (LHCP). When a circular polarization is considered, the electric field has two linear component, with equal magnitude while the direction changes in a rotatory manner due to a phase difference of $\pi/2$ [4].

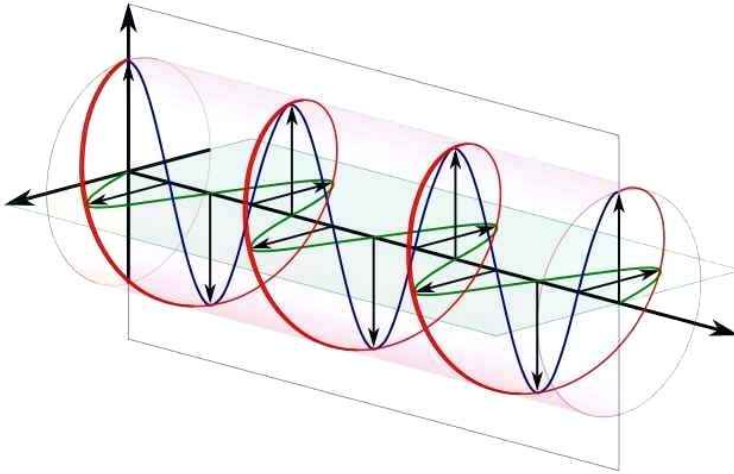


Figure 5.24. Circular Polarization

The circular polarization is defined from the source to the transmitter. Right and left circular polarization are defined in two different ways. Pointing the thumb in the same direction of the wave propagation, the fingers in the direction of the field's temporal rotation, the field seems to rotated clockwise from the point of view of the source; this is a right-handed convention and it refers to RHCP. On the contrary, the LHCP is a left-handed convention and the is anti-clockwise.

As it is possible to see from the following figures, with this approach the reconstructed field is able to follow the profile of the reference, both for a right hand and for a left hand circular polarization. Best results are obtained when a spline trajectory is used.

An important result is obtained, different from the case of a regular surface, when a uniform $\lambda/2$ sampling is considered; in the case of an irregular surface, measuring the points as reported in Figure 5.15, both the Near Field and the Far field (Figure 5.25) are properly reconstructed, with a small error. Instead, when the points are

taken on a regular surface, as in Figure 5.7, the error is much high and the near field can't be computed according to that trajectory.

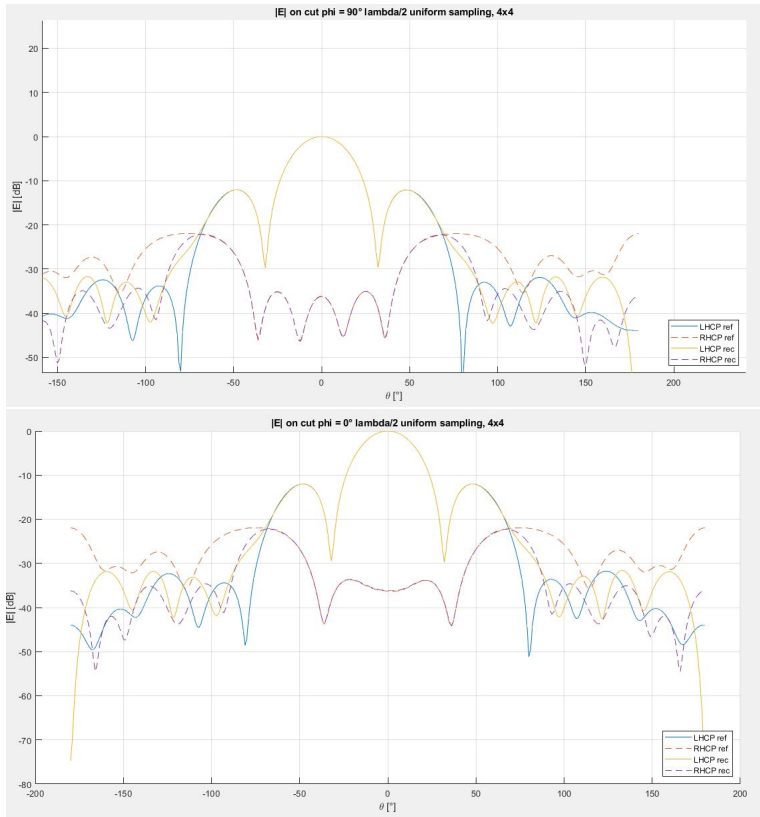


Figure 5.25. Original FF and reconstructed FF for a uniform $\lambda/2$ sampling

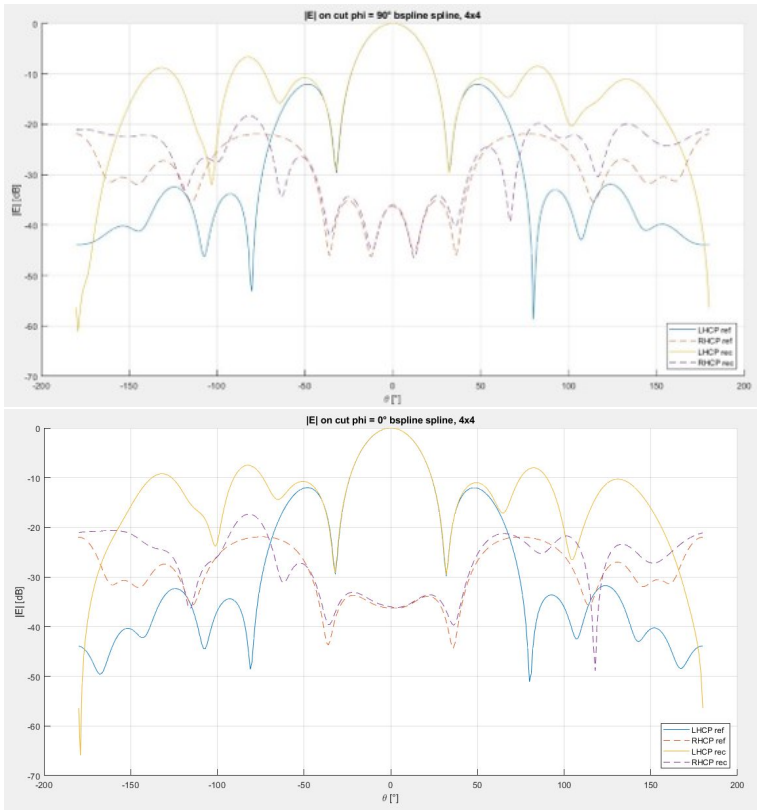


Figure 5.26. Original FF and reconstructed FF for B-spline trajectory

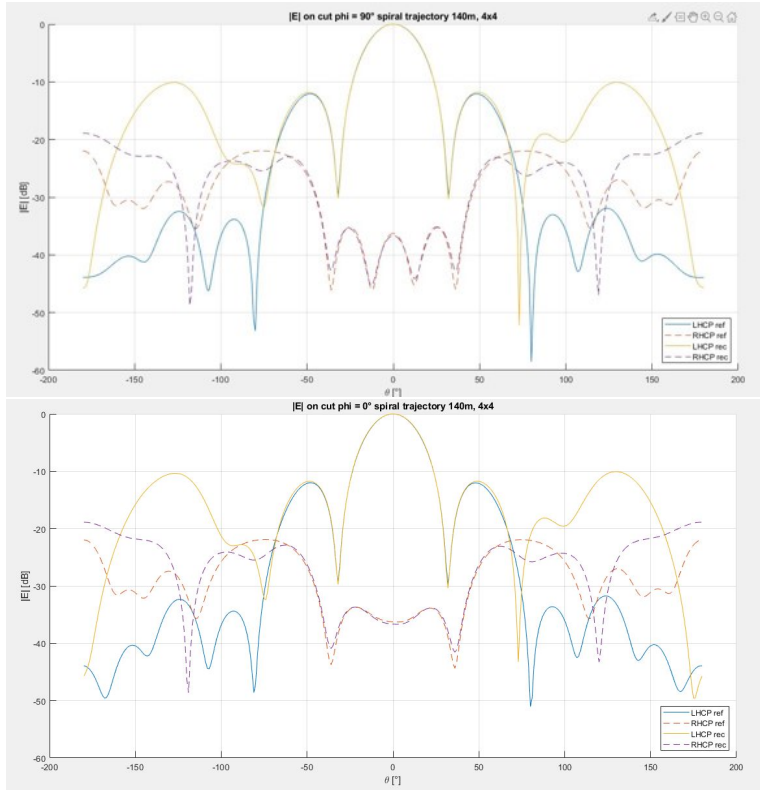


Figure 5.27. Original FF and reconstructed FF for spiral trajectory, 140m

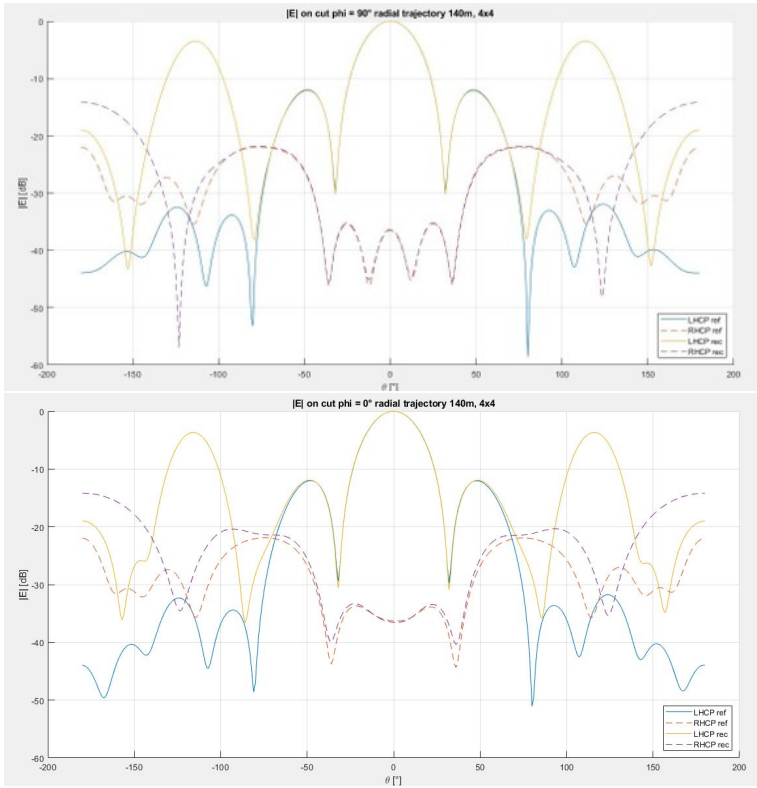


Figure 5.28. Original FF and reconstructed FF for radial trajectory, 140m

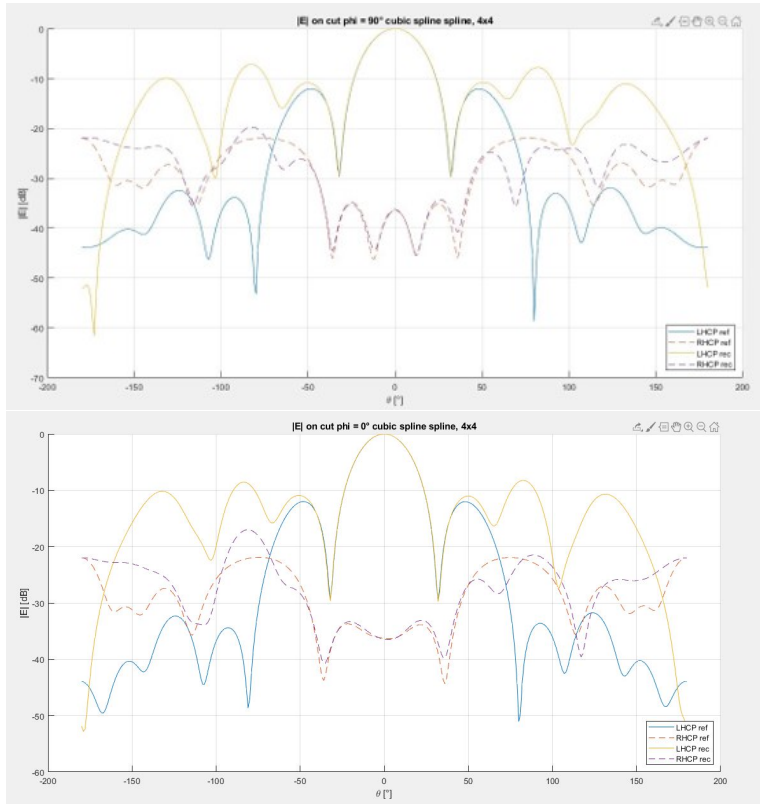


Figure 5.29. Original FF and reconstructed FF for cubic trajectory

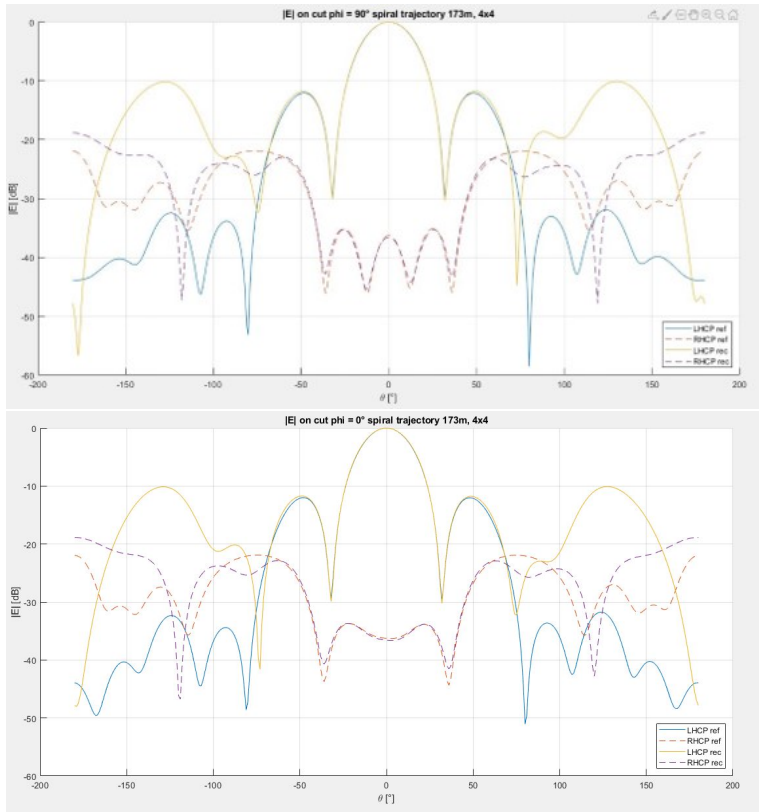


Figure 5.30. Original FF and reconstructed FF for spiral trajectory, 173m

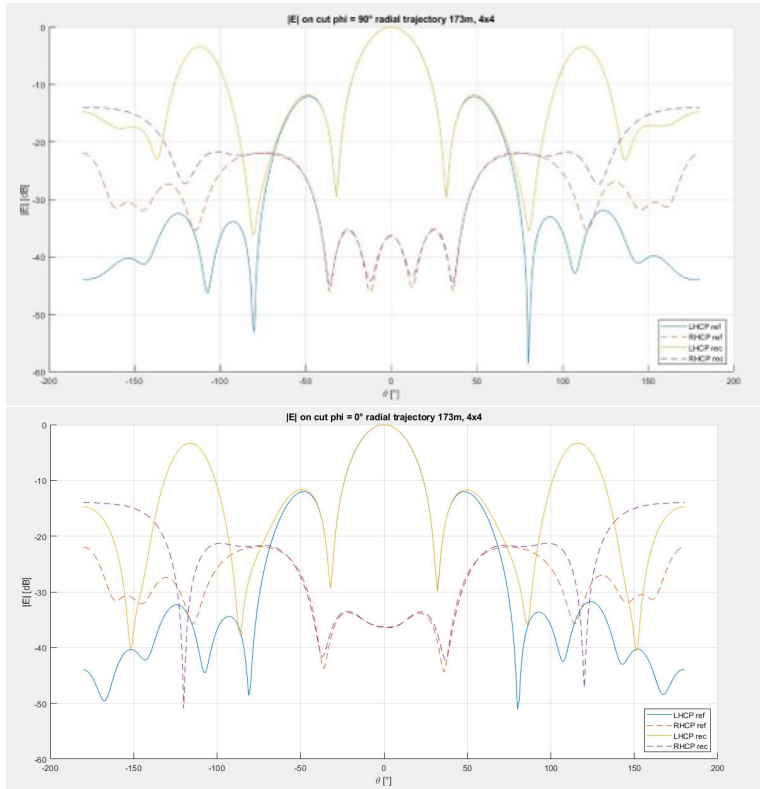


Figure 5.31. Original FF and reconstructed FF for radial trajectory, 173m

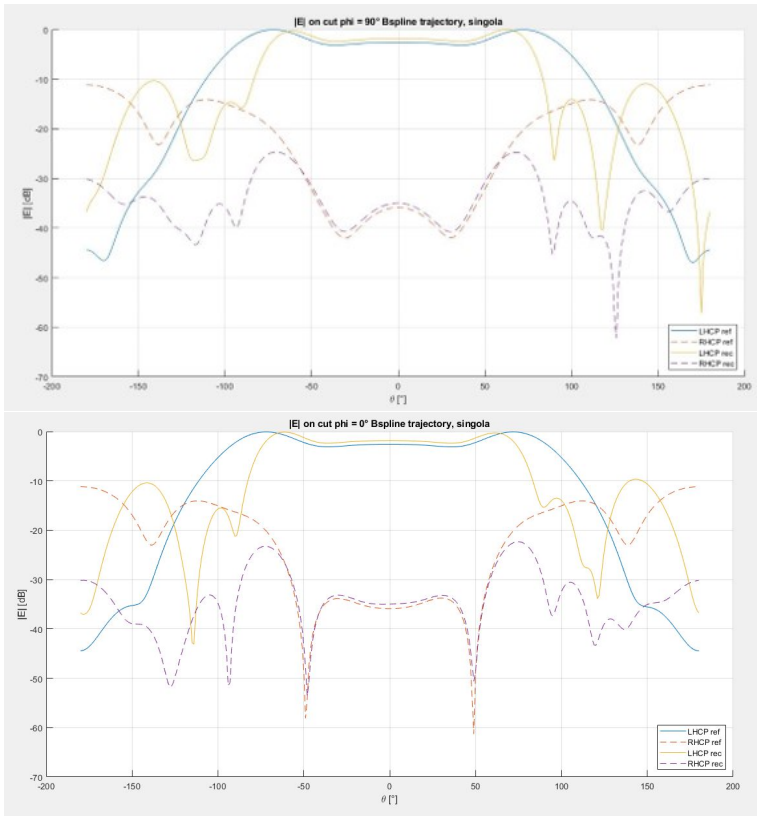


Figure 5.32. Original FF and reconstructed FF for B-spline trajectory, single antenna

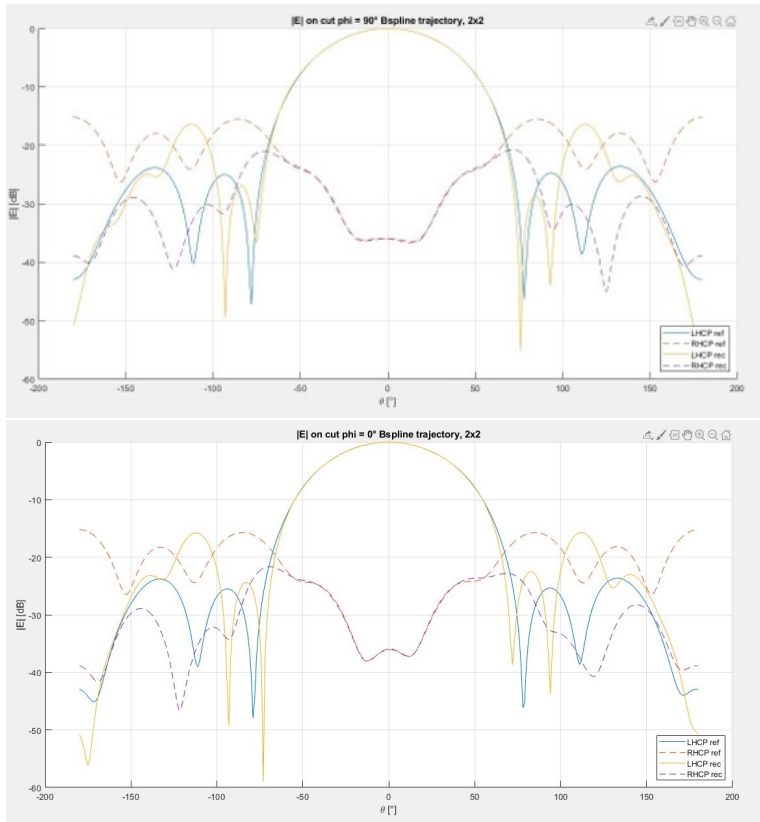


Figure 5.33. Original FF and reconstructed FF for B-spline trajectory, array 2x2

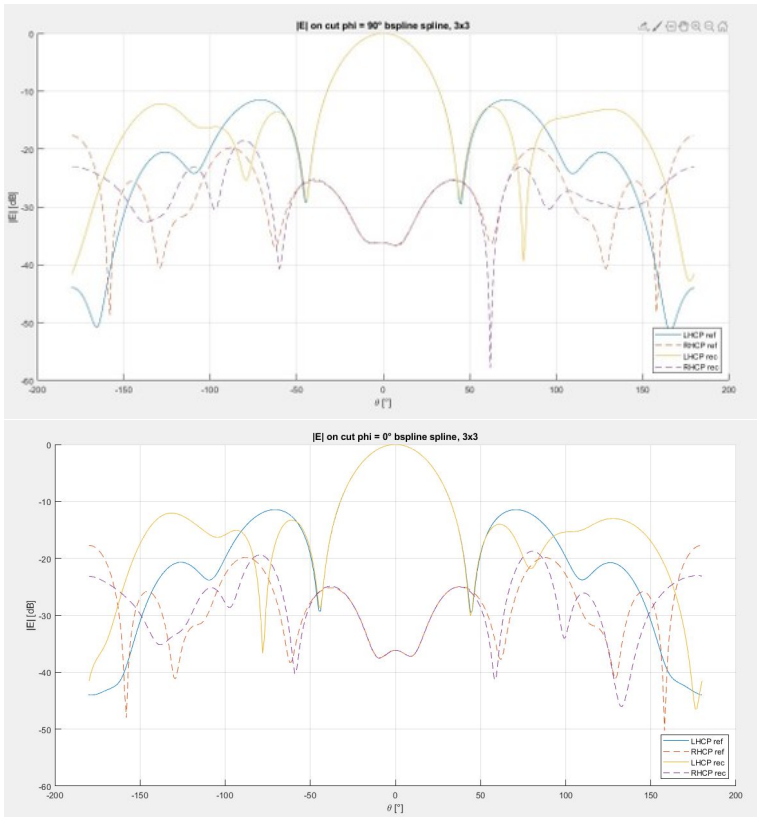


Figure 5.34. Original FF and reconstructed FF for B-spline trajectory, array 3x3

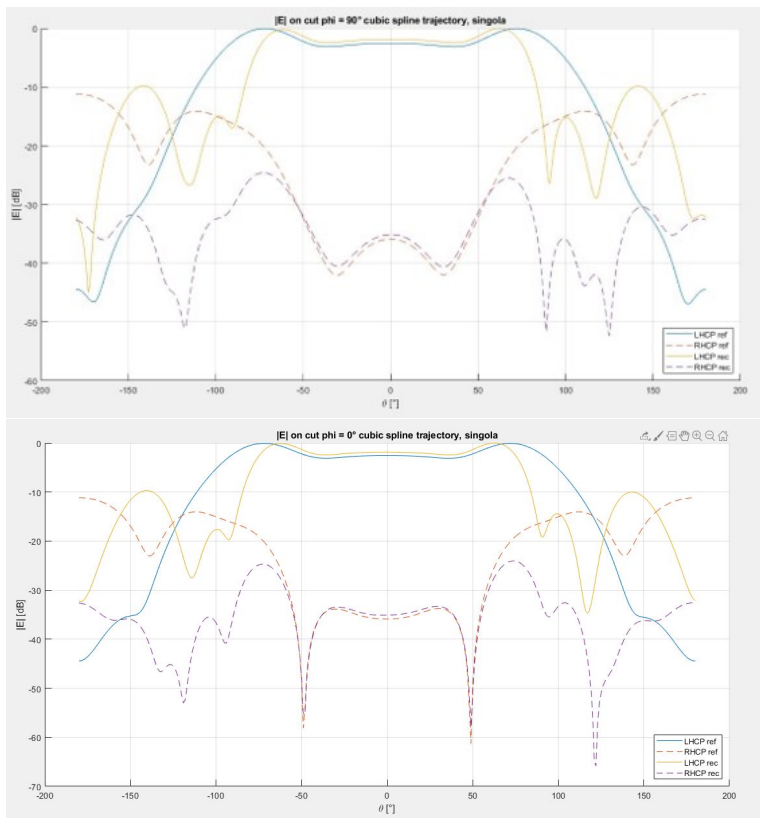


Figure 5.35. Original FF and reconstructed FF for cubic spline, single antenna

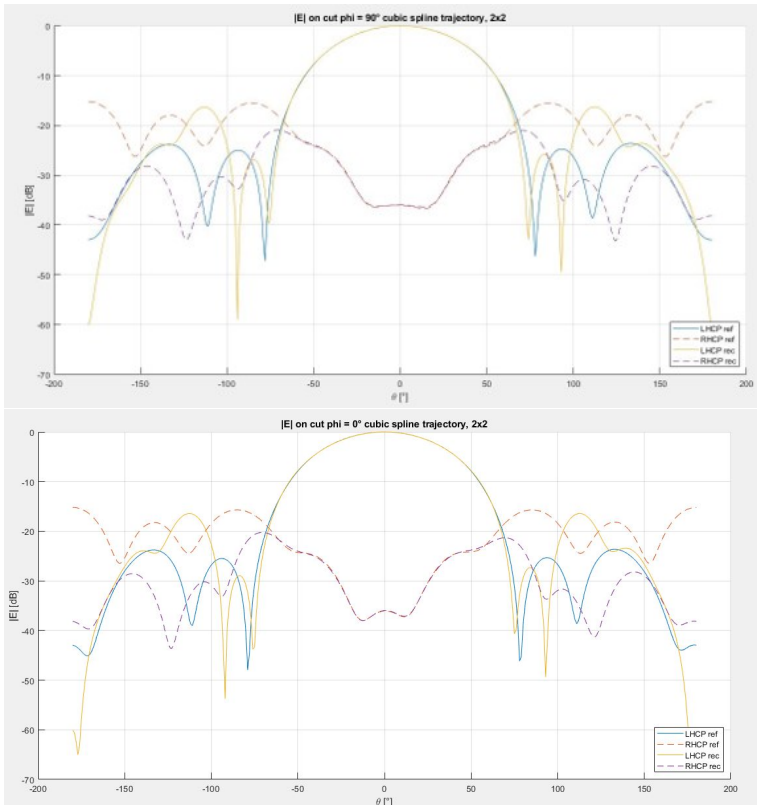


Figure 5.36. Original FF and reconstructed FF for cubic spline, array 2x2

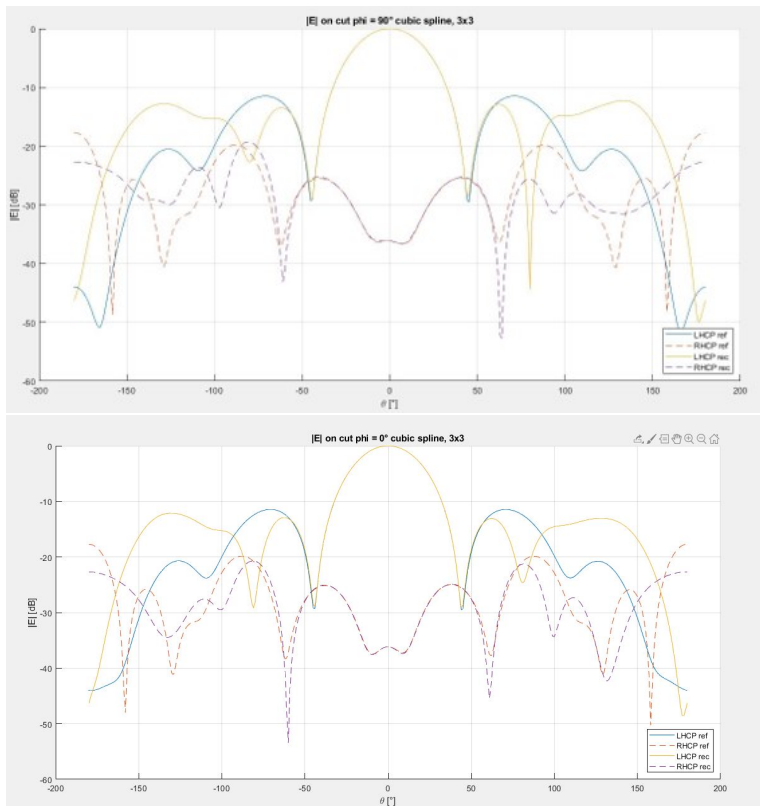


Figure 5.37. Original FF and reconstructed FF for cubic spline, array 3x3

Chapter 6

CONCLUSION

As seen in the previous chapters, the method that gives the best results in terms of the error of the reconstruction of the field is the reduced order model. The only drawback is due to the computational time in order to get the radiation matrix, \mathbf{G} ; it depends from the number of measured points and on the size of the surface that encloses the radiating object. The more are big these quantities, the more is the time needed for getting \mathbf{G} . It is important to underline again that by using the ROM, with the knowledge of the equivalent currents, it is possible to compute both the radiated near and far field. If only a fast characterization is needed the best method is the use of the SVT algorithm, since it is possible to manage with a huge amount of data in a very fast way. The CVX software works well if the points are selected randomly (as done in the starting paper [15]).

Regarding to the trajectories of the drone, if the aim is to use a method of the completion matrix the best path for the drone is the radial one, since the error is smaller than the case of the spiral; instead, if the ROM is used, the best way is to

determine the points that corresponds to the dominant equivalent currents with the DEIM, determine the minimum path between the desired amount of points that we want to visit and find a B-spline trajectory; the B-spline trajectory is preferred to the cubic spline since it is smoother and shorter. Anyway, this kind of work should be improved by approaching to a more realistic problem step by step. For example, it may be considered a real flight simulation where the drone doesn't fly at constant height; or can be considered the case when the measurement can be affected by the error of the sensor in the drone or can be affected by external noises of the environment.

Bibliography

- [1] MS Neiman. The principle of reciprocity in antenna theory. *Proceedings of the IRE*, 31(12):666–671, 1943.
- [2] John Leonidas Volakis, Richard C Johnson, and Henry Jasik. *Antenna engineering handbook*. 2007.
- [3] HJ Riblet. Note on the maximum directivity of an antenna. *Proceedings of the IRE*, 36(5):620–623, 1948.
- [4] Robert C Hansen and Robert E Collin. *Small antenna handbook*. Wiley Online Library, 2011.
- [5] Roger F Harrington. Effect of antenna size on gain, bandwidth, and efficiency. *J. Res. Nat. Bur. Stand*, 64(1):1–12, 1960.
- [6] Robert S Elliot. *Antenna theory and design*. John Wiley & Sons, 2006.
- [7] Donald L Lee and DL Lee. *Electromagnetic principles of integrated optics*. Wiley New York (NY) et al., 1986.
- [8] Peter Monk et al. *Finite element methods for Maxwell's equations*. Oxford University Press, 2003.
- [9] WW Hansen. A new type of expansion in radiation problems. *Physical review*, 47(2):139, 1935.

- [10] George B Arfken and Hans J Weber. *Mathematical methods for physicists*, 1999.
- [11] Magdy F Iskander. *Electromagnetic fields and waves*. Waveland Press, 2013.
- [12] C Cronström. A simple and complete lorentz-covariant gauge condition. *Physics Letters B*, 90(3):267–269, 1980.
- [13] Jørgen Hald and Frank Jensen. *Spherical near-field antenna measurements*, volume 26. Iet, 1988.
- [14] Leopold B Felsen. Evanescent waves. *JOSA*, 66(8):751–760, 1976.
- [15] Benjamin Fuchs, Laurent Le Coq, and Marco Donald Migliore. On the interpolation of electromagnetic near field without prior knowledge of the radiating source. *IEEE Transactions on Antennas and Propagation*, 65(7):3568–3574, 2017.
- [16] MJD Powell. The uniform convergence of thin plate spline interpolation in two dimensions. *Numerische Mathematik*, 68(1):107–128, 1994.
- [17] Emmanuel J Candès and Benjamin Recht. Exact matrix completion via convex optimization. *Foundations of Computational mathematics*, 9(6):717, 2009.
- [18] Vassilis Kalofolias, Xavier Bresson, Michael Bronstein, and Pierre Vandergheynst. Matrix completion on graphs. *arXiv preprint arXiv:1408.1717*, 2014.
- [19] Maryam Fazel. *Matrix rank minimization with applications*. 2002.
- [20] Jian-Feng Cai, Emmanuel J Candès, and Zuowei Shen. A singular value thresholding algorithm for matrix completion. *SIAM Journal on optimization*, 20(4):1956–1982, 2010.
- [21] Amit Hochman, Jorge Fernández Villena, Athanasios G Polimeridis, Luís Miguel Silveira, Jacob K White, and Luca Daniel. Reduced-order models

- for electromagnetic scattering problems. *IEEE Transactions on Antennas and Propagation*, 62(6):3150–3162, 2014.
- [22] Benjamin Fuchs and Athanasios G Polimeridis. Reduced order models for fast antenna characterization. *IEEE Transactions on Antennas and Propagation*, 67(8):5673–5677, 2019.
- [23] William B Johnson. Factoring compact operators. *Israel Journal of Mathematics*, 9(3):337–345, 1971.
- [24] Gene H Golub and Christian Reinsch. Singular value decomposition and least squares solutions. In *Linear Algebra*, pages 134–151. Springer, 1971.
- [25] Michael Jünger, Gerhard Reinelt, and Giovanni Rinaldi. The traveling salesman problem. *Handbooks in operations research and management science*, 7:225–330, 1995.
- [26] James M Keller, Michael R Gray, and James A Givens. A fuzzy k-nearest neighbor algorithm. *IEEE transactions on systems, man, and cybernetics*, (4):580–585, 1985.
- [27] Carl De Boor, Carl De Boor, Etats-Unis Mathématicien, Carl De Boor, and Carl De Boor. *A practical guide to splines*, volume 27. springer-verlag New York, 1978.
- [28] Luigi Biagiotti and Claudio Melchiorri. *Trajectory planning for automatic machines and robots*. Springer Science & Business Media, 2008.
- [29] Luigi Biagiotti and Claudio Melchiorri. B-spline based filters for multi-point trajectories planning. In *2010 IEEE International Conference on Robotics and Automation*, pages 3065–3070. IEEE, 2010.